Seismotectonics of the thick-skinned Santa Bárbara System in northwestern Argentina: implications for regional crustal rheology and structure

Martin Zeckra[1,2], Frank Krüger[1], R. Germán Aranda Viana[3], Fernando Hongn[3], Federico Ibarra[1,4], Jonathan R. Weiss[1,5] and Manfred R. Strecker[1]

[1]Institute of Geosciences, University of Potsdam, Karl-Liebknecht-Str. 24-25, 14476 Potsdam-Golm, Germany.

[2]Now at Royal Observatory of Belgium, Avenue Circulaire, 3, BE1180 Brussels, Belgium

[3]Instituto de Bio y Geociencias del NOA, Universidad Nacional de Salta-CONICET, 9 de Julio 14, 4405 Rosario de Lerma, Salta, Argentina,

[4] Instituto Geográfico Nacional, Buenos Aires, Argentina

[5]Now at NOAA/NWS/Pacific Tsunami Warning Center, 1845 Wasp Boulevard, Building 176, Honolulu, Hawaii, 96816, USA

Abstract

The Andean foreland is divided into morphotectonic provinces characterized by diverse deformation styles and seismogenic behavior partially stemming from distinct geological histories that preceded the current phase of subduction. The transition between the high Andes

and the eastern foreland is exposed to numerous natural hazards and contains critical economic infrastructure, yet we know relatively little about regional active tectonics due to few geophysical investigations. Here we use waveforms collected during a 15-month-long seismic network deployment in the Santa Bárbara System (SBS) of northwest Argentina following the 2015 M_w 5.7 El Galpón earthquake to determine the distribution and magnitude of local earthquakes, obtain a regional 1D seismic velocity model, and improve our overall understanding of SBS neotectonics. Of the nearly 1200 recorded earthquakes, ~700 occurred in the crust with half of the moment release associated with events deeper than 25 km. The depth extent of seismicity supports the notion that the SBS upper and middle crust are homogeneous and that the lower crust is composed of granulites. These conditions likely formed during Paleozoic mountain building and Salta Rift-related Cretaceous magmatism, which dehydrated the crust. We find no clear indications that a shallow, low-angle detachment fault inferred to have been active during Cretaceous rifting exerts a strong control on modern deformation in contrast to the active décollement beneath the adjacent fold-and-thrust belt of the Subandes to the north. It remains unclear how active, inverted normal faults in the SBS shallow crust connect to the deeper zones of seismicity.

Plain Language Summary

The actively deforming eastern flank of the central Andean plateau in southern Bolivia and northwest Argentina (NWA) contains tectonic structures such as faults that host moderate-sized yet damaging earthquakes in a region with large population centers and critical economic infrastructure. The area is also the youngest part of the longest mountain chain in the word and of particular interest for investigating how mountains grow. However, it remains unclear how north-

47 south variations in the region's geologic history and style of subduction influence modern-day
48 deformation. Here we use the distribution of seismicity recorded after the 2015 M_w 5.7 El Galpón
49 earthquake by a temporary network of seismic instruments to better understand the crustal
50 structure and rheology of the Santa Bárbara System (SBS) in NWA and to address debates
51 regarding the role pre-existing structures play in accommodating active deformation. Our key
52 finding is that most earthquakes occurred in the middle to lower crust extending towards the
53 crust-mantle boundary whereas relatively little seismicity was associated with shallow faults.
54 This finding supports the idea that deep rocks in the SBS are dry due to earlier phases of
55 deformation/magmatism and can support brittle deformation at temperatures normally too high
56 for earthquakes to occur.
57
58 **Key Points**

59 - Temporary seismic network deployment reveals new details regarding seismotectonics of
60 the thick-skinned Andean foreland in NW Argentina
61 - Half of the moment release recorded in the seismicity catalog is associated with events
62 deeper than 25 km
63 - Abundant deep seismicity points to an anhydrous, granulitic lower crust that formed
64 during Cretaceous rifting and magmatism

65
66 **1. Introduction**
67 The Subandean ranges of southern Bolivia and northwestern Argentina (Figure 1) are associated
68 with wedge-shaped, thin-skinned fold-and-thrust belts that are well-described from geometrical

and mechanical perspectives by critical taper theory [e.g., *Dahlen*, 1990; *Dahlen et al.*, 1984; *Davis et al.*, 1983]. Critical taper theory posits that the form of an orogenic wedge is controlled by the mechanical properties of the rocks involved in the deformation, the depth and geometry of a basal décollement, foreland basin geometry, and the ratio between tectonic deformation (i.e., shortening) rate and climatically controlled erosional mass flux [*Willett*, 1999]. When not at steady state, an orogenic wedge can thicken via out-of-sequence deformation on internal structures or widen by foreland-directed lateral growth of the mountain belt, with a well-developed deformation front at the wedge tip, where active thrust faults link with the underlying décollement [*Hilley and Strecker*, 2004; *Weiss et al.*, 2018; *Willett*, 1999].

Southward, the Subandes (SA) transition into the Santa Bárbara System (SBS), which is characterized by uplift of basement-involved uplifted fault blocks, often associated with the inversion of Cretaceous normal faults [*Arnous et al.*, 2020; *Barcelona et al.*, 2014; *Jordan et al.*, 1983; *Kley and Monaldi*, 2002; *Mon and Salfity*, 1995; *Ramos et al.*, 2006]. This thick-skinned style of deformation continues farther south to the Sierras Pampeanas (SP) morphotectonic province, which is characterized by reverse-fault bounded basement blocks [*Jordan et al.*, 1983; *Ramos*, 2000]. In contrast to the SA, the SBS has not developed systematically from west to east and lacks a well-defined frontal deformation zone. Instead, the SBS forms an extensive, tectonically active province with spatially isolated and diachronous uplifts reflected by an unsystematic, fault-controlled river network [*Seagren et al.*, 2022; *Strecker et al.*, 2012].

Major differences between the thin- and thick-skinned sectors of the Andean foreland also exist with respect to geodetically determined, decadal-scale deformation patterns. For example,

92 instead of the steep gradient in horizontal surface velocity documented across the SA [e.g.,
93 *Brooks et al.*, 2011; *Weiss et al.*, 2016], GPS data from the thick-skinned sectors including the
94 SBS and adjacent Eastern Cordillera and Andean Plateau morphotectonic provinces display a
95 gradual decrease in horizontal surface velocities from west to east [*Figueroa et al.*, 2021]. This
96 decrease suggests a kinematic style that might be related to either a deep-seated, rheology-
97 controlled décollement, multiple detachment levels, the complete lack of basal low-angle
98 faulting, faulting across isolated and widely distributed steep, basement-cored faults, or a
99 combination of these factors.
100
101 Previous work in the SBS and the adjacent Andean interior has greatly improved our
102 understanding of the seismicity and deep structure of the orogen [e.g., *Cahill et al.*, 1992; *Devlin*
103 *et al.*, 2012; *Mulcahy et al.*, 2014; *Schurr et al.*, 1999; *Schurr et al.*, 2003; *Whitman et al.*, 1992;
104 *Wimpenny et al.*, 2018], but relatively little is known about the active tectonics and seismological
105 characteristics of the upper and middle crust. For example, the suggestion that the broken
106 foreland is part of the SA orogenic wedge and underlain by a shallow, westward-dipping
107 décollement is based solely on structural cross-section balancing [*Grier et al.*, 1991; *Kley and*
108 *Monaldi*, 2002; *Pearson et al.*, 2013]. Furthermore, although Quaternary deformation in the SBS
109 and adjacent Eastern Cordillera is widespread, the seismogenic nature of faults and associated
110 deformation features is not well established [*Arnous et al.*, 2020; *Barcelona et al.*, 2014;
111 *Figueroa et al.*, 2021; *García et al.*, 2019]. More detailed geophysical information is needed to
112 better characterize the Andean foreland crust, to test structural models that seek to explain the
113 broken foreland deformational style, and to accurately assess regional seismic hazard.
114

To address this lack of information, we deployed the temporary **STRATEGy** (**S**eismic Ne**T**wo**R**k/**A**rray in Nor**T**hw**E**stern ar**G**entina) seismic network [*Zeckra and Kruger*, 2016] following the October 17, 2015 M_w 5.7 El Galpón earthquake in the southern part of the SBS (Figure 1). Our principal aims were to (1) identify the causative earthquake fault, (2) determine the depth distribution of seismicity, and (3) use the retrieved earthquake data to improve our understanding of deformation patterns in the SBS compared to adjacent morphotectonic provinces. Importantly, the spacing between STRATEGy network stations near the epicenter of the El Galpón event was one tenth of those in the permanent Argentinian national network [*Sánchez et al.*, 2013], enabling us to record elevated aftershock microseismicity and regional background seismicity with a detection threshold two orders of magnitude lower than the regional network. The STRATEGy network was also uniquely positioned above a seismic gap in the underlying subducting Nazca plate and between zones of intermediate- and deep-focus, subduction-related earthquakes (Figure 1) [*Cahill and Isacks*, 1992].

Here, we present results from the STRATEGy seismic network deployment. We describe the semi-automatic post-processing procedure used to generate a local earthquake catalog including hypocenter locations, local magnitudes (*ML*), and focal mechanisms. We also derive a new 1D regional seismic velocity model for the Central Andean foreland crust. The relocated event hypocenters provide new insights into regional crustal structure and rheology and permit a reevaluation of various structural and seismotectonic models proposed for the SBS broken-foreland province and back-arc region in general.

2. Tectonic setting

138 The SBS is a morphotectonic province located between approximately 23° S and 27° S to the
139 east of the Andean Plateau (known in Argentina as the Puna Plateau), the internally drained high-
140 elevation interior of the orogen, and the abutting thick-skinned thrust belt of the Eastern
141 Cordillera that extends along the eastern border of the Puna Plateau (Figure 1). The SBS is a
142 tectonically active broken foreland [*Jordan et al.*, 1983; *Ramos*, 2000] characterized by
143 diachronous range uplift and deformation [*Alvarado and Ramos*, 2011; *Arnous et al.*, 2020;
144 *Carrera and Muñoz*, 2008; *Hain et al.*, 2011; *Mon and Salfity*, 1995; *Ramos et al.*, 2006; *Strecker*
145 *et al.*, 2012]. Fault-controlled topography in this region is primarily the result of the contractional
146 Cenozoic inversion of normal faults that formed during Cretaceous extension [*Marquillas et al.*,
147 2005; *Mon and Salfity*, 1995]. In contrast, in the broken foreland of the Sierras Pampeanas (SP),
148 located between approximately 27° and 33° S [*Jordan et al.*, 1983], shortening is accommodated
149 along deep-rooted reverse faults associated with reactivated Paleozoic basement shear zones,
150 rather than extensional structures [*Bellahsen et al.*, 2016; *Cristallini et al.*, 2004; *Jordan and*
151 *Allmendinger*, 1986; *Ramos et al.*, 2002].
152
153 Although deformation rates in the transition zone between the Eastern Cordillera and the SBS are
154 generally low [*Figueroa et al.*, 2021; *García et al.*, 2019; *McFarland et al.*, 2017], Quaternary
155 fault scarps, folds, and tectonic landforms attest to ongoing activity [*Arnous et al.*, 2020; *Kley*
156 *and Monaldi*, 2002; *Mon*, 1976; *Mon and Gutiérrez*, 2007] and document sustained, possibly
157 seismogenic, foreland deformation and compartmentalization into smaller sub-basins [*Arnous et*
158 *al.*, 2020; *Barcelona et al.*, 2014; *Ramos et al.*, 2006]. Strain release in the form of small- to
159 intermediate-size earthquakes also characterize the SBS and adjacent EC [e.g., *Cahill and Isacks*,
160 1992; *Sánchez et al.*, 2013]. For example, in the past decade, two severe earthquakes resulting in

161 human casualties have occurred in this region: the 2010 M_w 6.3 Salta and the 2015 M_w 5.7 El
162 Galpón earthquakes [*García et al.*, 2013; *Scott et al.*, 2014; *Zeckra*, 2020] (Figure 1). Historical
163 seismicity records further show that this slowly deforming portion of the Andean foreland
164 experiences earthquakes with long recurrence intervals and estimated magnitudes of up to M 7
165 [*Costa et al.*, 2020; *Ortiz et al.*, 2021; *Perucca and Moreiras*, 2009; *Zossi*, 1979]. Despite the
166 regional seismic hazard potential, previous temporary seismic array deployments have focused
167 primarily on large-scale imaging of the boundary between the subducting Nazca and overriding
168 South American plates as well as the investigation of geodynamical processes including those
169 associated with the Puna Plateau [e.g., *Asch et al.*, 2006; *Cahill and Isacks*, 1992; *Laske et al.*,
170 2013; *Schurr et al.*, 1999; *Whitman*, 1994; *Whitman et al.*, 1992]. Relatively little is known about
171 the seismotectonics of the broken foreland.
172
173 **3. Data and Methods**
174 *3.1 The STRATEGy seismic network deployment*
175 In mid-2016 we installed the temporary STRATEGy seismic network across the SBS, which
176 consisted of 13 seismic stations that recorded earthquake activity for a period of 15 months. The
177 primary aim of the survey was to characterize local and regional seismicity to provide new
178 insight into active tectonics, crustal deformation, and seismic hazard. The network covered a 110
179 x 58 km area with an average interstation spacing of ~20 km (Figure 2). We focused on areas of
180 potentially recent active faulting based on previous geological, seismological, and geophysical
181 investigations [e.g., *Cahill et al.*, 1992; *Iaffa et al.*, 2013; *Iaffa et al.*, 2011; *Kley and Monaldi*,
182 2002; *Kley et al.*, 1999; *Whitman et al.*, 1992] in combination with observations from our pilot
183 fieldwork in 2016. We also established our network near the epicenter and in the aftermath of the

2015 M_w 5.7 El Galpón earthquake and the adjacent Cerro Colorado and Sierra de La Candelaria (Figure 2). Three main criteria were considered when determining the locations of the seismic stations: (1) minimizing the depth to bedrock to improve sensor coupling and ensure a wideband signal spectrum, (2) maximizing remoteness as the signal-to-noise ratio is proportional to distance from anthropogenic ambient noise sources, and (3) maximizing security so that seismic stations were preferentially located within sight of nearby settlements to avoid disruptions or security problems.

Each station was equipped with a Lennartz 3D5s seismometer (flat response to ground velocity for frequencies between 0.2 Hz and 50 Hz), except for station 14A, which was equipped with a Mark L-4C-3D short-period sensor. The analog 100 Hz data output was digitized using 23-bit Type 2 DATA-CUBE3 digitizers and stored internally. The power supply came from batteries connected to solar panels. All equipment apart from the solar panels and the external GPS antennas required for accurate time synchronization was buried for protection from heat, insolation, precipitation, and animals. The seismic sensors were buried 0.6 m beneath the surface and oriented towards magnetic north. One exception was station 03B, which was placed in a 2-m-deep concrete vault that formerly housed a regional seismic network site.

A laboratory-based instrument validation test was performed with all seismic sensors prior to the network installation and repeated after dismantling. Based on the input-output cross-spectrum of two sensors with highly correlated signals it is possible to infer the sensors transfer functions [*Havskov and Alguacil*, 2004]. No instrument bias due to alteration of components from previous

206 experiments could be identified. The post-survey tests also ensured instrument parameter
207 consistency during the recording period.
208
209 In addition to the data from our network, the Argentinian Seismological Service INPRES
210 (Instituto Nacional de Prevención Sísmica) provided us with continuous waveform data from two
211 permanent seismic network stations [*Sánchez et al.*, 2013] that served to enhance our network
212 coverage (Figure 2). The two stations, separated by 230 km, are located close to the cities of
213 Tucumán (AHML) and Salta (SLA) and are 159 km and 119 km from the El Galpón earthquake
214 epicenter, respectively. Station SLA is equipped with three short-period (nominally 1.0 Hz)
215 Geotech Model S-13 sensors to capture motion in 3 dimensions. A similar vertical-component
216 seismometer exists in Tucumán together with a 3-component Guralp CMG-40 broadband
217 seismometer. Both INPRES permanent stations are equipped with satellite communications, but
218 data transmission was unreliable during the survey period resulting in repeated small gaps in the
219 archived data. Clock synchronization errors also affected the permanent stations; we therefore
220 implemented an automated static time offset correction (STOC) method to identify and correct
221 the associated errors (see Supporting Information S1).
222
223 Variable lithology, structural geometry, and subsurface characteristics across our study area affect
224 the appearance of recorded waveforms. Stations 01B, 02A and 05A were located within the
225 Metán Basin (Figure 2), which contains up to 4.5 km of Cenozoic sediments with corresponding
226 alluvial fans in the piedmont of the Sierra de La Candelaria, where unconsolidated sediments rest
227 on the shallow bedrock. Stations 03A and 04A were located on Cretaceous and early Tertiary
228 sedimentary bedrock, respectively. Station 14A was located on steeply dipping, gypsum-bearing

lithified strata of marine origin. Despite being located on bedrock within a concrete vault, the waveforms recorded at station 03B show perturbations due to topographic effects because of its elevated position. There are no detailed geological descriptions of the subsurface rheology in the vicinity of stations 06A and 07B.

Several of the stations did not provide continuous recordings over the entire 15-month-long deployment. For example, station 02A recorded for only 158 days before it was stolen. The power supply at station 13A was disrupted by farm animals resulting in a 32-day data gap. Major recording gaps were also associated with high-rainfall conditions during the austral summer months [*Bookhagen and Strecker*, 2008; *Ramezani Ziarani et al.*, 2019; *Strecker et al.*, 2007]. Extreme rainfall events led to complete technical failure for many stations due to corrosion of batteries or charge controllers. The rainfall also limited access to the remote stations and their repair could only be carried out after the monsoon season. Additional information related to network ambient seismic noise levels and associated seasonal variations can be found in the Supporting Information (Figures S1 and S2).

3.2 Seismic Data Processing

Processing and analysis of the seismic data was performed using a semi-automated workflow aimed at minimizing subjectivity while preserving reproducibility and efficacy of statistical uncertainty analysis. We used flexible, open-source python libraries dedicated to seismological data processing including Pyrocko [*Heimann et al.*, 2019], Obspy [*Beyreuther et al.*, 2010], and MTfit [*Pugh and White*, 2018]. We also used QuakeML, an XML-based data exchange standard

format for seismology [*Schorlemmer et al.*, 2011], for data storage and to ensure that the entire processing chain associated with the final earthquake catalog could be documented.

3.2.1 Event Detection

Unsupervised event detection is less time consuming than manual scanning of continuous waveform data and preserves a high degree of objectivity in the analysis at the cost of reducing the level of precision. We apply the delay-and-stack method [*Cesca and Grigoli*, 2015; *Grigoli et al.*, 2013], which enables exploitation of the full, continuous waveforms using coincidence information from the whole network. This method is applicable for analyzing a wide range of seismological data associated with processes including volcano-tectonic deformation [*Drew et al.*, 2013; *Langet et al.*, 2014], landslides [*Hibert et al.*, 2014], and induced seismicity [*Comino et al.*, 2017; *Grigoli et al.*, 2013] and is implemented in the Lassie automated full waveform detector [*Comino et al.*, 2017; *Heimann et al.*, 2019]. In the case of the STRATEGy network, the method enables the simultaneous detection of seismic events with a high variability in source-receiver path lengths, focal depths, and waveform characteristics. The unsupervised approach uses arbitrary source locations in a predefined gridded volume (2.5 km cell size) to estimate theoretical arrival times for each station in the network, along which the characteristic functions of the recorded waveforms are stacked. The internal ray-tracer Cake calculates theoretical arrival times for direct P- and S-phases based on a layered-earth model on a spherical Earth. In this step we use the 1D velocity model from the Swiss Seismological Service that was built for a mountainous region and an adjacent foreland basin [*Husen et al.*, 2003] because no comparable velocity model existed for the SBS prior to our study. The application of characteristic functions onto the band-passed waveform data (1 – 15 Hz for P-phases, 1 – 8 Hz for S-phases) removes

possible bias due to radiation patterns of the double couple seismic sources and differs for the two seismic phases; STA/LTA (short term average = 1 s, long term average = 8 s) for the sharper P-phase onsets and moving average functions for the more emergent S-phases. The latter induces a strong smoothing, so the resolvability of the source depth vanishes, and the original source volume was reduced to a single horizontal layer at the surface to achieve additional computational efficiency. Finally, the detection trigger is activated after thresholding (threshold = 100) the dimensionless resulting stacked characteristic functions.

3.2.2 Phase picking

Further seismic waveform analysis to estimate event locations and magnitudes depends on accurate identification of seismic phases and their onset times. The list of events detected by Lassie in the previous step provides a robust indicator of time windows within the continuous data stream that contain seismic signals. To accurately determine seismic phase onsets, we use the autoregression phase-picking algorithm implemented in the ObsPy library [*Beyreuther et al.*, 2010] in combination with a coincidence trigger to analyze the identified time windows only at stations that recorded the earthquake. We verified the automatically derived results by manually re-picking events using the dynamic waveform visualization tool Snuffler implemented in Pyrocko (Figure S3). In this step we also assign the polarity of first-motion arrivals for focal mechanism estimation (see section 3.5).

3.2.3 Event location

We use HYPOSAT [*Schweitzer*, 2001] to locate the earthquakes identified in the previous steps based on the arrival times and travel-time differences of direct, reflected, and critically refracted seismic wave phases [*Storchak et al.*, 2003]. A variety of spherical Earth velocity models are available for event location determination but we use AK135 [*Kennett et al.*, 1995], a standard global model for continental regions. Local deviations from this global velocity model within the source region, defined as within a 1.5° radius around the earthquake epicenter, were captured using the CRUST 1.0 model [*Laske et al.*, 2013]. This procedure is largely unsupervised except for the definition of the *a priori* starting depth of 25 km in the HYPOSAT inversion, which is deeper than global averages in continental areas [*Sloan et al.*, 2011] but resulted in more stable and accurate hypocenter estimation in our study area.

3.2.4 Earthquake magnitude estimation

We estimate the magnitudes of earthquakes in our catalog using the updated IASPEI local magnitude (*ML*) scale [*Bormann and Dewey*, 2012]

$$ML = log_{10}A + 1.11log_{10}R + 0.00189R - 2.09 \quad (1)$$

where A is the maximum horizontal trace amplitude measured on a Wood-Anderson instrument and R is the hypocentral distance. The *ML* equation also contains three empirically determined constants, which we derived using the calibration function determined for Southern California that is also used by INPRES [*Sánchez et al.*, 2013] so that our results would be comparable to the national earthquake catalog. The final event magnitude is the mean of all individual station magnitudes calculated using Equation 1 on bandpass (0.1 – 30 Hz) filtered, Wood-Anderson simulated displacement seismograms. As the *ML* value was determined for events with

hypocentral distances <1000 km, earthquakes at greater distances were excluded from the fully automated magnitude estimation routine but remain in the catalog with no assigned magnitudes.

3.3 Local 1D velocity model determination

An accurate local seismic velocity model provides a realistic representation of subsurface rheological properties and elastic parameters and helps reduce hypocenter location uncertainties. To derive a 1D velocity model for the SBS we use VELEST [*Kissling et al.*, 1994] and a catalog subset of 215 well-located crustal earthquakes, which we define as events with confirmed P- and S-phase arrivals recorded at a minimum of six stations and with an azimuthal gap smaller than 180°. VELEST solves the coupled hypocenter-model problem by minimizing travel-time residuals using the root-mean-square-misfit. Each step in the inversion yields a solution consisting of an earthquake hypocenter, station corrections, and a 1D velocity model. VELEST inverts for layer velocities only and not for layer thicknesses or the number of layers. Therefore, we use a trial-and-error approach to determine the best layered model set-up for the P-wave velocity only, since this component is subject to lower uncertainties and yields more stable solutions. We arrive at our preferred model by performing stability tests that include varying the initial hypocenter location (random, by 5 and 10 km), resampling the catalog (20, 50, 100 events randomly omitted), and creating geographical subsets that broadly correspond to variations in local geology. These tests permit exploration of weighting schemes for different layers and help stabilize the inversion for layers crossed by a small number of ray paths (e.g., at mantle depths or in the shallow sedimentary layer). The final velocity model (see Section 4.2; Table 1; Figure 5) is constructed from layer-wise averaging of the best 10% of 5000 model runs. We simultaneously invert for P- and S-wave velocities and calculate V_P/V_S ratios from the individual model

outcomes. We down-weight S-wave arrival times by 50% and dampen the respective station correction by a factor of 2.0 in contrast to a factor of 0.1 for the P-wave station corrections. This scaling accounts for the greater uncertainties associated with the emergent character of the S-wave arrivals. VELEST hypocenter solutions deviate from the starting locations by a few kilometers at most so we chose not to use them to update the event catalog.

3.4 Double-difference relocation

A major challenge to using seismological data to derive a high-resolution image of seismotectonic structures and processes is large hypocenter location uncertainties. As mentioned earlier, refining the local velocity model helps reduce the absolute location errors of well-defined hypocenters. Location accuracy can be further improved using inter-event travel-time differences. We use the joint hypocenter determination method implemented in HypoDD [*Waldhauser and Ellsworth*, 2000], which simultaneously minimizes the travel time difference uncertainty of two linked events located <12 km apart observed at two seismic stations (i.e., double-differencing) across the catalog of 8,371 event pair combinations. The inclusion of >3,000 cross-correlation differential phase arrival times further increases the location accuracy of 408 events.

3.5 Focal mechanism determination

In addition to providing a basis for rigorous analysis of tectonic structures based on the spatial distribution of precisely located earthquakes, the first-motion polarity from single earthquake sources can be used to invert for earthquake focal mechanisms. We use MTfit [*Pugh and White*, 2018], which employs Bayesian inversion scheme to estimate the most likely source model in the

363 form of marginal probability density functions of the observation parameters (e.g., polarity and
364 amplitude). A Monte Carlo random sampling draws 2.5 million moment tensor solutions per
365 event that are reduced to three independent parameters (strike, dip, rake) by normalizing the
366 moment tensor and assuming double couple point sources for the pure tectonically induced
367 microseismicity [*Pugh et al.*, 2016]. Source–receiver paths are constructed from azimuth and
368 incidence angles using the Cake ray-tracer tool [*Heimann et al.*, 2019], the high-precision
369 HypoDD locations, and our new 1D seismic velocity model. Out of 208 earthquakes with an
370 azimuthal gap <180º we obtained 22 reliable focal mechanisms (Figure 4; Table S1).
371

372 **4. Results**

373 *4.1 Seismicity Catalog*

374 The earthquake catalog derived from the STRATEGy network deployment consists of 1919
375 automatically detected events throughout the 15-month recording period, resulting in an average
376 of ~4.3 events/day. However, due to heavy rainfall events, daily recorded seismicity was
377 inconsistent during the austral summer, resulting in a temporary decrease in the number of
378 operational stations and fewer recorded earthquakes (Figures S4 and S5). During the first five
379 months of recording with a full network, an average of 10±5 events/day was detected. This rate
380 gradually decreased over time until 0 events/day were recorded towards the end of the monsoon
381 season, when only three stations were operational. The time-dependent event decay rate based on
382 Omori's law [*Utsu et al.*, 1995] suggests that some of the events recorded early in the survey
383 were aftershocks of the 2015 M_w 5.7 El Galpón earthquake (see Supporting Information S2).
384 Following restoration of the damaged stations, the event-detection rate remained stable at three
385 events/day during the last four months of recording, presumably reflecting the background

386 seismicity rate. This value is higher than previous estimates not only for this area [*Cahill et al.*,
387 1992], but also for continental intraplate environments such as western Anatolia [*Akyol et al.*,
388 2006] and parts of Central Asia [*Schurr et al.*, 2014; *Sippl et al.*, 2013], and is closer to values
389 found near active plate boundaries such as New Zealand and the Himalayas [*Michailos et al.*,
390 2019; *Monsalve et al.*, 2006].
391
392 We determined the hypocenter locations and *ML* for 1435 earthquakes. After excluding 236
393 events with a fixed depth, we generated a refined catalog of 1199 earthquakes with assigned
394 hypocenter uncertainties. We then categorized earthquakes with local (<100 km) to regional
395 (<1000 km) epicentral distances into three distinct groups: (1) shallow crustal earthquakes at
396 depths <50 km, (2) intermediate-depth earthquakes within the Wadati-Benioff Zone at a depth of
397 ~200 km, and (3) deep earthquakes located at depths >500 km (Figures 1, 2, and S6).
398
399 Of the latter, earthquakes with a hypocentral depth of ~600 km align along a narrow band
400 striking nearly north-south located to the east of the orogen (Figure 1). The largest magnitude,
401 non-teleseismic event in our catalog falls into this category (date: 20170221; origin time:
402 14:09:07.7 UTC; depth: 646 km*; ML* 7.3; M_W 6.5). Intraslab activity within the Wadati-Benioff
403 zone of the subducting Nazca Plate is restricted to the northwest corner of our network beneath
404 the Andean Plateau. This area of seismic activity has previously been referred to as the “Jujuy
405 Nest" [*Cahill and Isacks*, 1992; *Kirby et al.*, 1996; *Mulcahy et al.*, 2014; *Valenzuela-Malebrán et*
406 *al.*, 2022] (Figure 1) and is thought to be associated with dehydration of the subducting plate and
407 the partial melting of the overlying asthenospheric wedge [*Kirby et al.*, 1996; *Schurr et al.*,

2003]. Crustal earthquakes with *ML* 0.5-4.6 are confined to the Eastern Cordillera and the Central Andean foreland. Recorded seismic activity diminishes northward towards the SA but broadens to the south toward the SP. Importantly, the earthquake hypocenters are distributed over the entire thickness of the crust down to the approximate depth of the Moho at 43 km [*Laske et al.*, 2013; *Tassara and Echaurren*, 2012] (See Section 4.3 and Figures 4 and 5).

Absolute hypocenter-location uncertainties, which we estimated while inverting for the source locations, are primarily related to source-receiver distances. Epicentral location errors are less than 10 km for events within 30 km of the network (Figure 3) and increase to tens of kilometers at regional distances <1000 km. Our estimates of focal-depth uncertainty for crustal earthquakes are limited to events within the STRATEGy network with azimuthal coverage <180°. Large uncertainties around station AHML reflect time-synchronization errors. The application of double-difference relocation for 408 local earthquakes within the network lowered their theoretical location uncertainty by a factor of 1000 compared to the primary hypocenter estimations resulting in a median horizontal uncertainty of 2.8 m with 99% of the location uncertainties smaller than 10 m.

We obtained a magnitude of completeness (M_C) for the investigated area of 1.45 using the b-value stability approach [*Woessner and Wiemer*, 2005]. Separating local and regional crustal events yields M_C values of 1.3 and 2.1, respectively. The M_C values of 2.6 and 3.6 for intermediate-depth and deep-focus events are below the INPRES catalog M_C of 3.9 for events in the study area over the same time. The overall detection limit (minimum observable magnitude)

increases linearly with hypocentral distances >45 km and by one earthquake magnitude for every 303 km increase in hypocentral distance. Station magnitude residuals follow normal distributions (Figure S7) with mean values reflecting station site characteristics and shallow subsurface lithology. For example, positive residuals are related to amplification effects within the intermontane Metán Basin due to the thick layer of unconsolidated sediments, whereas negative residuals are associated with stations located on or close to bedrock.

Recorded earthquakes at mid- to lower-crustal depths (~25-40 km) are widely scattered throughout the study area (Figures 2 and 4). The base of the zone of lower-crustal seismicity is sub-horizontal and dips gently northwestward, reaching depths close to the Moho beneath the Eastern Cordillera (Figure 4). Earthquakes located at depths greater than ~25 km are responsible for approximately half of the moment release during the observation period (Figure 5). This is consistent with the relatively low b-value of 0.75 calculated from the earthquake magnitude-frequency distribution and the suggestion that deeper hypocenters tend to be associated with larger magnitude events [*Amitrano*, 2003; *Mori and Abercrombie*, 1997].

The upper crust at depths shallower than ~25 km appears to be mostly aseismic across the Eastern Cordillera-Santa Bárbara System transition (i.e., beneath the Sierra de Metán in the northern SBS and the Sierra del Brete and the Choromoro Basin in the southern SBS; Figure 3). Moving eastward towards the foreland, however, shallow, low-magnitude earthquakes are most likely associated with upper crustal structures in the Metán Basin, beneath the Cerro Colorado as well as beneath and north of the Sierra de La Candelaria (Figure 4b and c). This shallow

seismicity transitions with increasing depth to pronounced zones of earthquake activity concentrated around the M_w *5.7* El Galpón and *ML* 5.3 Rosario de la Frontera earthquake hypocenters (Figures 2 and 4). These events occurred prior to the installation of our temporary network and many of the recorded earthquakes are likely aftershocks (see below). The first cluster is in the north in the vicinity of the 2015 M_w 5.7 El Galpón event, and the aftershocks appear to occur along one of the suggested fault plane solutions, aligning nearly north-south and extending over a wide depth range roughly coincident with a steep, east-dipping fault plane. Aftershocks extend down to a depth of ~30 km, which is generally deeper than global continental averages for teleseismically-determined earthquake focal depths [e.g., *Sloan et al.*, 2011]. The second cluster is likely associated with the *ML* 5.3 earthquake that occurred on September 5, 2015, approximately 47 km south of the El Galpón earthquake epicenter. The location uncertainties associated with this cluster are too high to definitively relate it to any seismotectonic structures, and the distribution recorded with the temporary network supports both N-S- or E-W-striking fault orientations. The absence of moment-tensor solutions for the *ML* 5.3 event prevents any further first-order source characterization due to its small magnitude. Overall, mid- to lower-crustal seismicity is more diffuse in the southern portion of the SBS than in the north.

4.2 Regional distribution of events

The Metán Basin appears to play an important role in controlling both the along-strike structural segmentation of the SBS [*Kley and Monaldi*, 2002] and the observed seismicity (Figures 2 and 4). South of the basin, Proterozoic metamorphic basement rocks are exposed at the surface,

forming the nucleus of the Sierra de La Candelaria, for example, and only a few reverse faults cut the crust. In contrast, the exposed strata north of the basin are generally younger and primarily west-verging faults outcrop at the surface. There are also subtle, but distinct differences in the spatial distribution of earthquake hypocenters, although our dataset captures seismicity primarily surrounding and to the south of the Metán Basin with some deeper events extending to the north (Figures 1 and 2). Shallow seismicity essentially terminates just north of the Garrapatas transfer zone and in map view the hypocenters concentrate around the edges and particularly to the east of both the Metán and Choromoro Basins (Figure 2). Seismicity generally shallows approaching the eastern edges of these basins, with deeper events located beneath the central Metán Basin, the Sierras de Metán and La Candelaria. More abundant seismicity characterizes the crust beneath the Metán Basin and the Cerro Colorado range, particularly at mid-crustal depths where a broad peak in the depth distribution of seismicity centered at ~18 km is observed (Figure 5). The largest cluster of events is found beneath the surface trace of the Metán Basin Central Thrust Fault [MBCTF; *Iaffa et al.*, 2011] and is likely associated with the aftershock sequence of the El Galpón earthquake. Seismicity is far less abundant beneath Sierra de La Candelaria, and there is no distinct peak in the depth distribution of the events; earthquake hypocenters are evenly distributed throughout the crust to a depth of ~30 km (Figure 5).

4.3 1D velocity model

Our final 1D velocity model (Table 1; Figure 5) consists of five layers including two shallow sedimentary layers, an upper and lower crust, and the upper mantle. We divide the shallow sediments into upper, unconsolidated, and lower, compacted layers, which are resolvable based

496 on contrasting P-wave velocities and a significant difference in the V_P/V_S ratio. The lack of
497 crossing ray paths associated with deeper-than-average focal depths likely results in greater
498 velocity uncertainties in the shallow sediments compared to the other layers. For the shallow
499 sediments, rock properties such as porosity, pore-fluid pressure, and strength influence seismic
500 velocity [*Lee*, 2003]. Previously recognized regional lithological variations [*Iaffa et al.*, 2011]
501 are reflected in the station velocity residuals of the stations compared to average subsurface
502 velocities. For example, station 05A located in the center of the sediment-filled Metán Basin
503 yields very high S-wave residuals of ~1.4 seconds. The S-wave velocities in the shallow layers
504 are better constrained than the P-wave velocities. Hence, the large V_P/V_S ratio uncertainties are
505 primarily due to the V_P estimates. Our results confirm the presence of strong lateral and vertical
506 lithological heterogeneities in the shallow subsurface (i.e., unconsolidated basin fill on top of and
507 adjacent to fault-bounded, metamorphic basement rock) throughout the study area.
508
509 The upper crust of the SBS, in contrast, is largely homogeneous and characterized by constant
510 velocity between the depths of 4 and 33 km. The upper crustal V_P/V_S ratio of 1.76 is close to the
511 value obtained using our dataset and a Wadati diagram [*Zeckra*, 2020] (Figure S8). A substantial
512 increase in V_S at a depth of 33 km and an associated reduction in V_P/V_S to an abnormally low
513 value [*Christensen*, 1996] characterizes the transition from the upper to the lower crust.
514 Additional variations in the seismic velocities of the SBS crust cannot be ruled out, but
515 additional rheological information (e.g., temperature, heat flux, stress, density) is required to
516 resolve finer details (Figure 4).
517

518 The Moho is delineated by an increase in V_P, V_S, and V_P/V_S at a depth of 43 km, which is an
519 approximate depth since only a few ray paths penetrate the crust-mantle boundary. The low
520 uncertainty beneath this depth results from strong damping of the mantle velocity variations in
521 the inversion bounded by values from tomographic studies and global velocity models [*Laske et*
522 *al.*, 2013] as only a few ray paths penetrate the crust-mantle boundary.

523

524 At shallow crustal levels our new velocity model compares favorably with global models such as
525 AK135 and CRUST1.0 [*Kennett et al.*, 1995; *Laske et al.*, 2013]. With increasing depth,
526 however, our inverted velocity values are generally lower and the layer boundaries deeper than
527 the global estimates. For example, the Moho is situated 2.6 and 8 km deeper than the CRUST1.0
528 and AK135 models, respectively. We suggest that our 1D model provides an enhanced regional
529 picture of the crust and upper-mantle velocity compared to the global estimates.

530

531 **5. Discussion**

532 *5.1 Proposed crustal fault geometries versus broken foreland seismicity*

533 Three decades ago *Grier et al.* [1991] suggested that compressional inversion and reactivation of
534 Cretaceous Salta Rift extensional structures including shallow (listric) normal faults and a basal
535 sub-horizontal shear zone representing the brittle-ductile transition (i.e., the principal
536 detachment) at a depth of 10-12 km exerts a primary control on foreland basin and fault
537 geometries during Cenozoic contractional Andean orogenesis. Subsequent studies [e.g., *Cahill et*
538 *al.*, 1992; *Cristallini et al.*, 1997; *Iaffa et al.*, 2011; *Kley and Monaldi*, 2002] generally support
539 this interpretation with proposed modifications of the detachment level and number of

detachments. While reactivation of inherited basement heterogeneities is generally accepted as an important mechanism during the tectonic evolution of basement-uplift provinces, the link between the activity of surface structures and motion along deep-seated crustal heterogeneities is the subject of ongoing debate [e.g., *Ammirati et al.*, 2022; *Bellahsen et al.*, 2016; *Brooks et al.*, 2003; *Lacombe and Bellahsen*, 2016; *Ramos et al.*, 2004].

In the SBS there is structural evidence for reactivation and inversion of normal faults [e.g., *Abascal*, 2005; *Cristallini et al.*, 1997; *Iaffa et al.*, 2013; *Iaffa et al.*, 2011; *Kley and Monaldi*, 2002; *Kley et al.*, 1999; *Kley et al.*, 2005; *Mon and Salfity*, 1995] but the distribution of crustal earthquakes recorded during our network deployment is only partially compatible with these observations. At depths ≤10 km, sparse earthquake hypocenters lie in the vicinity of a closely spaced series of reverse and inverted normal faults beneath the Cerro Colorado and the Metán Basin (Figure 4). A few shallow earthquakes also occurred beneath the Sierra de la Candelaria and in close proximity to the surface trace the MBCTF [*Iaffa et al.*, 2011], which may have hosted the 2015 M_w 5.7 El Galpón earthquake; a down-dip extrapolation of the steep, near-surface portion of the MBCTF passes through the El Galpón hypocenter. However, most relocated shallow events do not cluster along continuous planes that coincide with the location of shallow faults, nor can the earthquakes be easily projected from the surface to deeper depths (Figure 4).

Structural cross sections tend to place the base of recently active faults at ~15 km where they are interpreted to intersect the low-angle detachment horizon even though the maximum penetration depth of regional seismic reflection data is ~8 km [e.g., *Iaffa et al.*, 2011]. There is a distinct

563 peak in the relocated seismicity depth distribution histogram at ~12 km (Figure 5) but in cross-
564 section only a few events coincide with the inferred location of the detachment (e.g., directly
565 beneath the MBCTF and beneath and to the east of the Sierra de la Candelaria; Figure 4)
566 suggested by *Grier et al.* [1991]. Thus, the proposed connection between the low-angle shear
567 zone that facilitated Cretaceous extension and present-day seismicity is unclear. This apparent
568 disconnect is in line with recent numerical modeling results that suggest pure-shear, thick-
569 skinned deformation is required to explain the structural evolution of the SBS [*Liu et al.*, 2022]
570 in contrast to the simple shear, detachment-involved, thin-skinned tectonics that characterize the
571 SA. Furthermore, a recent reevaluation of the GPS-derived, horizontal surface velocity field
572 [*Figueroa et al.*, 2021] questions the notion that a shallow décollement beneath the SBS controls
573 deformation [e.g., *McFarland et al.*, 2017] and instead suggests that structures such as a much
574 deeper, rheology-controlled décollement, multiple detachment levels or the complete lack of
575 basal low-angle faulting and faulting across isolated and widely distributed steep basement
576 faults, or a combination of these factors are more likely. If the inherited rift-related structures and
577 a basal detachment control SBS contractional deformation, we would expect a clearer link
578 between these features and the relocated earthquakes at shallow and/or mid- to lower-crustal
579 depths.
580
581 The lack of correspondence may be partially due to the limited duration of our seismic network
582 deployment. Most crustal earthquakes recorded in our study occur around the 2015 epicenters
583 and near the eastern limits of the SBS despite the lack of a well-defined deformation front and
584 elongate thrust fault-related structures (Figure 2). We suspect that the map-view seismicity
585 pattern is a transient feature characteristic of active broken-foreland provinces, where localized

586 deformation on reverse faults that are short in map view increases stress-loading on adjacent
587 structures until they fail, resulting in non-systematic patterns of deformation [e.g., *Hilley et al.*,
588 2005]. A similar deformation style, with spatially separate and diachronous reverse-fault
589 bounded range uplifts, has been ascribed to the Cretaceous Laramide province of North America
590 [*Marshak et al.*, 2000] and the Cenozoic Tien Shan of Central Asia [*Burbank et al.*, 1999; *Liu et*
591 *al.*, 2022]. Future regional seismic deployments would likely capture different earthquake spatial
592 patterns including events that might align more closely with some of the shallow structures.
593 However, the correspondence between the distribution of Cretaceous rift-related sediments and
594 the earthquake hypocenters (Figures 1 and 2) points to inherited rheological control [e.g.,
595 *Wimpenny*, 2022].
596
597 *5.2 Implications for crustal composition and structure of the SBS*
598 The earthquake hypocenter distribution involves nearly the full extent of the continental crust
599 (Figures 4 and 5), which has significant implications for the overall crustal structure and
600 rheology of this portion of the orogen. The base of seismicity terminates abruptly in the lower
601 crust and dips gently westward; the deepest relocated events are located ~10 km above the Moho
602 in the eastern SBS and are at or slightly above the Moho approaching the Eastern Cordillera in
603 the west (Figure 4). The general lack of deeper hypocenters suggests the presence of a boundary
604 akin to a brittle-ductile transition just above the Moho.
605
606 The homogeneous seismic velocity within the upper crust (Figure 5) indicates low heat flow
607 comparable to cratonic environments [*Currie and Hyndman*, 2006]. This characteristic might be
608 partially explained by underthrusting of the old and cold Brazilian Shield, which has been related

609 to the large degree of SA shortening [*Allmendinger and Gubbels*, 1996; *Babeyko and Sobolev*,
610 2005; *Gubbels et al.*, 1993; *Kley et al.*, 1996; *Lamb*, 2000; *Liu et al.*, 2022], although there are no
611 unambiguous indications that this process influences SBS deformation. The 1D seismic
612 velocities also suggest the existence of a felsic mid-crustal layer with lower than global average
613 velocities [*Christensen and Mooney*, 1995]. This interpretation is compatible with recently
614 published thermal, strength, and rheological models [*Ibarra et al.*, 2019; *Ibarra et al.*, 2021] in
615 addition to well logs from the La Candelaria region [*Arnous et al.*, 2020].
616
617 Seismicity that extends across the entire crust implies brittle deformation at temperatures as high
618 as ~600º C [Figure 5; *Sloan et al.*, 2011], which contrasts the standard view of crustal seismicity,
619 where the quartzo-feldspathic lower crust is hydrous, weak, and aseismic beneath a shallow,
620 temperature-controlled, brittle-ductile (i.e., seismic-aseismic) transition at 300-350ºC [*Maggi et*
621 *al.*, 2000; *Scholz*, 1998; *Sibson*, 1982]. Deep seismicity at elevated temperatures is related to an
622 anhydrous lower crust [*Jackson et al.*, 2004; *Yardley and Valley*, 1997]. Such environments are
623 typically associated with partial melting of granites, related magmatism at temperatures of ~700º
624 C, and the formation of metastable mafic granulites, which remain strong and brittle at elevated
625 temperatures [e.g., *Jackson et al.*, 2008; *Jackson et al.*, 2004; *Maggi et al.*, 2000]. Examples of
626 such environments are the Himalayan collision zone, where the Indian Shield is underthrusting
627 Tibet [e.g., *Copley et al.*, 2011; *Craig et al.*, 2012], and the southern East African Rift System
628 (EARS), where rift-related magmatic dehydration of the lower crust and associated changes in
629 lower crustal composition that support deep brittle deformation have been inferred [*Craig and*
630 *Jackson*, 2021; *Jackson et al.*, 2008; *Maggi et al.*, 2000].
631

632 The regional temperature and stress conditions that promote deep brittle deformation beneath the
633 SBS are best explained in the context of Mesozoic extensional tectonism and magmatism that
634 generated an anhydrous lower crust (i.e., similar to portions of the modern-day EARS) and the
635 subsequent evolution toward contractional tectonics during Cenozoic Andean orogenesis. The
636 rheological properties and geological history of the SBS are markedly different than the
637 seismically quiet, thin-skinned SA. The conditions that drive SBS deformation are more akin to
638 the thick-skinned SP to the south where seismicity occurs along fault planes that extend across
639 the entire crust and are believed to be reactivated crustal heterogeneities including Proterozoic or
640 Early Paleozoic sutures and/or Late Paleozoic or Mesozoic graben normal faults. The seismicity
641 ceases where the structures are inferred to intersect a shear zone at or slightly above the Moho
642 that may represent the main Andean décollement, which facilitates the eastward transfer of
643 Andean shortening to the SP [*Bellahsen et al.*, 2016; *Lacombe and Bellahsen*, 2016; *Ramos*,
644 1988; *Ramos et al.*, 2002; *Smalley Jr. et al.*, 1993]. It is worth noting that there is also evidence
645 in the SP for regional granulite facies metamorphism related to Paleozoic orogenesis and a
646 resulting anhydrous lower crust [*Rapela et al.*, 2010; *Wimpenny*, 2022].
647
648 The notion that the SBS lower crust is compositionally unique and anhydrous is supported by the
649 presence of granulite xenoliths of granitic and mafic composition retrieved from dikes and sills
650 intruded into the Cretaceous syn-rift sediments of the Salta Rift at about 90 Ma [*Galliski and*
651 *Viramonte*, 1988; *Gioncada et al.*, 2010; *Lucassen et al.*, 1999; *Viramonte et al.*, 1999].
652 Granulite-xenolith thermobarometry suggests equilibration temperatures of 850-900°C and
653 pressures that correspond to a depth of ~35 km [*Lucassen et al.*, 1999]. The petrologic evidence
654 documents contemporaneous mafic volcanism and granulite-facies metamorphism in the realm

655 of the Salta Rift at depths >30 km during Cretaceous extension. Although mafic granulites
656 account for only ~5% of all known granulitic xenoliths [*Lucassen et al.*, 2007; *Lucassen et al.*,
657 2005; *Lucassen et al.*, 1999] and the total addition of mafic melts to the crust may be limited
658 [*Franz et al.*, 2006], large portions of the lower crust beneath the Salta paleo-rift are likely mafic.
659 The portions of the SBS that were affected by Cretaceous melting or metamorphism-related
660 depletion of hydrous minerals now host deep brittle deformation. These conditions may even
661 apply to areas where volcanism was not dominant and where limited extensional faulting was
662 only associated with coeval deep-seated emplacement of magmatic dikes and sills, as suggested
663 by observations from other regions [e.g., *Behn et al.*, 2006; *Buck et al.*, 2005; *Tongue et al.*,
664 1992; Figure 6].
665
666 Estimates of the local yield strength envelope (YSE) indicate that the SBS lower crust is strong,
667 and that the brittle-ductile transition zone is located close to the Moho [*Ibarra et al.*, 2019;
668 *Wimpenny*, 2022] (Figures 4 and 5). The YSE shown in Figure 5c represents our preferred
669 scenario based on published regional thermal and density models [*Ibarra et al.*, 2019; *Ibarra et*
670 *al.*, 2021], our new velocity model (i.e., the anomalous lower crust V_P/V_S ratio), the associated
671 inferred rheology, and corresponding published values for coefficients of friction [e.g.,
672 *Christensen*, 1996; *Christensen and Mooney*, 1995; *Zoback et al.*, 1987]. More specifically, the
673 YSE was calculated by assuming that the upper crust is composed of quartz diorite, the lower
674 crust is granulitic based on xenolith composition and lower-than-average seismic velocities, and
675 the coefficient of friction is 0.1 based on the assumed presence of inherited crustal structures.
676 This combination of model parameters places the brittle-ductile-transition at a depth of ~38 km,
677 which is consistent with the depth distribution of recorded hypocenters but deeper than recent

678 geodynamical models that show high strain accumulation at the top of the lower crust and a
679 broad deformation zone extending into the mid-crust beneath the shallow faults [e.g., *Liu et al.*,
680 2022; Figure 6]. Our strength profile is also in line with results stemming from a recent
681 examination of the relationship between the distribution of Mesozoic rifts and seismicity along
682 the length of the Andean foreland, which suggests low effective coefficients of friction and the
683 presence of granulites in the lower crust to explain the deep seismicity in locations where ancient
684 rift basins exist [*Wimpenny*, 2022].
685
686 Elevated thermal gradients established during Cretaceous rifting, associated melting,
687 magmatism, and the formation of an anhydrous lower crust contrast sharply with the adjacent
688 SA, where no extensional processes have influenced the rheological properties of the crust. The
689 deep crustal earthquakes in the SBS are best explained by thermally controlled lithological and
690 compositional changes, as well as inherited structures, associated with Cretaceous rift-related
691 magmatic processes that caused an overall embrittlement of the lower crust. In this context it is
692 interesting to note that similar observations have been reported from the southeastern Colombian
693 Andes, which experienced lower crustal dehydration due to rifting and magmatism prior to
694 Cenozoic Andean mountain building [*Vásquez and Altenberger*, 2005; *Weber et al.*, 2002].
695 Evidence of these processes include mafic granulitic xenoliths retrieved from Cenozoic volcanic
696 rocks in the region, which is currently seismically active to depths of ~40 km [*Monsalve et al.*,
697 2019; *Taboada et al.*, 2000; *Wimpenny*, 2022].
698
699 *5.3 A revised seismotectonic model for the SBS*

Our temporary seismic network deployment installed after the 2015 El Galpón earthquake recorded abundant seismicity throughout the SBS crust. The resulting hypocenter distribution suggests the presence of two distinct zones of seismicity. Approximately one third of the recorded events occurred above a depth of ~20 km, in the general vicinity of steeply dipping faults, some of which are reactivated and inverted normal faults (Figure 4). The most likely interpretation is that Andean contractional deformation has reactivated the shallow basement heterogeneities/anisotropies and inverted some of the upper crustal faults. The widespread distribution of both recently active structures and seismicity in the foreland supports this view. Existing structural models suggest that the shallow faults root in a décollement that is similar in depth and related to the low-angle detachment fault that was active during Cretaceous extension when the Salta Rift sediments were deposited in different depocenters (Figure 1). However, our new seismicity observations in combination with the recent numerical modeling and geodetic results [*Figueroa et al.*, 2021; *Liu et al.*, 2022], suggest that the low-angle detachment fault does not play a decisive role in controlling compressional deformation in the SBS. The limited shallow seismicity agrees with modeling results that show minor strain accumulation in the vicinity of the shallow/inverted normal faults [e.g., *Liu et al.*, 2022; Figure 6]. The details of the relationship between the active/seismogenic shallow structures and the extension-related detachment fault remains unclear (Figure 6).

The remainder of the recorded seismicity occurred in the middle and lower crust. At depth, hypocenters terminate abruptly above the Moho across a sharp, sub-horizonal boundary that dips gently northwestward towards the Eastern Cordillera. Mid- and lower-crustal seismicity in the SBS is diffuse and does not delineate individual through-going structures.

723

724 Petrological data including the widespread distribution of mafic, granulite xenoliths indicate very
725 dry conditions at depths of several tens of kilometers. Thus, the SBS lower crust is anhydrous
726 and has experienced high-temperature metamorphism. These characteristics allow for the broad
727 distribution of present-day deep seismicity. The upper and middle crust comprise one
728 homogeneous layer extending down to a depth of ~33 km and likely consist of quartz diorite,
729 while the lower crust is composed of metastable and dry mafic granulites. Low heat flow and
730 low friction coefficients push the brittle-ductile transition zone to a depth of ~38 km.

731

732 **6. Conclusions**

733 We present a view of Andean foreland seismotectonics based on earthquakes recorded during a
734 15-month network deployment across the thick-skinned Santa Barbara System of Northwestern
735 Argentina in the aftermath of the 2015 M_w 5.7 El Galpón earthquake. Regional seismicity falls
736 into 3 general categories including shallow crustal events at depths <50 km, intermediate-depth
737 earthquakes at ~200 km related to subduction of the Nazca Plate beneath the Andes, and deep
738 earthquakes located at depths >500 km. We focus our attention on the crustal earthquakes and
739 find that brittle deformation is confined primarily to the easternmost, low-relief portion of the
740 Andean foreland. A double-difference relocation of the shallow microseismicity hints at activity
741 along steep reverse faults, many of which are reactivated structures formed during Cretaceous
742 extension and creation of the Salta Rift. The earthquake hypocenters extend to the Moho at a
743 depth of ~40 km before terminating in a sub-horizontal zone that is shallow in the east beneath
744 the range-front faults and deepens gradually westward approaching the high-topography Eastern
745 Cordillera and Puna Plateau. Half of the moment-release in the catalog is associated with

earthquakes below 25 km. The deep extension of the seismogenic zone and broadly distributed brittle deformation in the lower crust does not clearly delineate distinct structures extending from shallow depths. The observed homogeneous crustal composition inferred from modeled seismic velocities, unusually low V_P/V_S ratios, and petrologic evidence of granulite-facies rocks in the lower crust are consistent with Cretaceous rifting and associated magmatism that resulted in highly fractured, anhydrous conditions that promote deep seismogenesis. The transition from the adjacent, seismically quiet Subandean ranges in the north to the highly seismogenic Santa Barbara System is abrupt and associated with the distribution of Salta Rift related structures and associated magmatism. Map-view seismicity broadens southward crossing into the Sierras Pampeanas and associated large, range-bounding faults. The results from our local seismic network deployment help fill a gap in knowledge related to the seismogenic thickness of the Andean lithosphere and shed new light on the seismotectonics of an actively deforming broken foreland strongly influenced by the regional tectonic history.

Acknowledgments

The research was supported within the framework of the project IGK 2018 SuRfAce processes, Tectonics and Georesources: The Andean foreland basin of Argentina (StRATEGy) and funded by the Deutsche Forschungsgemeinschaft (DFG, grant to M.R. Strecker and F. Krüger STR 373/34-1) and the Brandenburg Ministry of Sciences, Research and Cultural Affairs, Germany. Field visits were furthermore supported by a Centro Universitario Argentino-Alemán grant (CUAA/DAHZ) by the German Academic Exchange Service (DAAD) to M.R.S. We thank the University of Potsdam for providing the seismic instrumentation and INPRES for providing access to waveform data for two of their stations. We also thank Municipalidad de El Galpón and

769 Instituto de Bio Y Geociencias del NOA (Conicet-UNSa) for logistical support. The earthquake
770 data from this study can be accessed through the ISC Seismological Dataset Repository at
771 https://doi.org/10.31905/YTIR1IED. The Generic Mapping Tools [GMT; *Wessel et al.*, 2013]
772 was used to create the figures presented in this paper.

773

774

775

776

777

778

779

780

781

782

783

layer	depth [km]	v_P [km/s]	v_S [km/s]	v_P/v_S
unconsolidated sediments	-3.0	4.16 ± 0.60	2.83 ± 0.11	1.45 ± 0.17
compacted sediments	1.5	5.71 ± 0.22	2.83 ± 0.11	2.02 ± 0.13
upper crust	4.0	5.81 ± 0.05	3.30 ± 0.04	1.76 ± 0.01
lower crust	33.0	6.65 ± 0.31	4.33 ± 0.08	1.54 ± 0.05
mantle	43.0	8.04 ± 0.07	4.49 ± 0.04	1.79 ± 0.02

784

785 **Table 1** Final minimum 1D velocity model. Velocities estimated from the median and standard
786 deviations of stable solutions at each layer from a uniform variety of starting models and
787 manually defined layer depths by merging layers of homogeneous velocities in initial, fine-grid
788 test models.
789
790

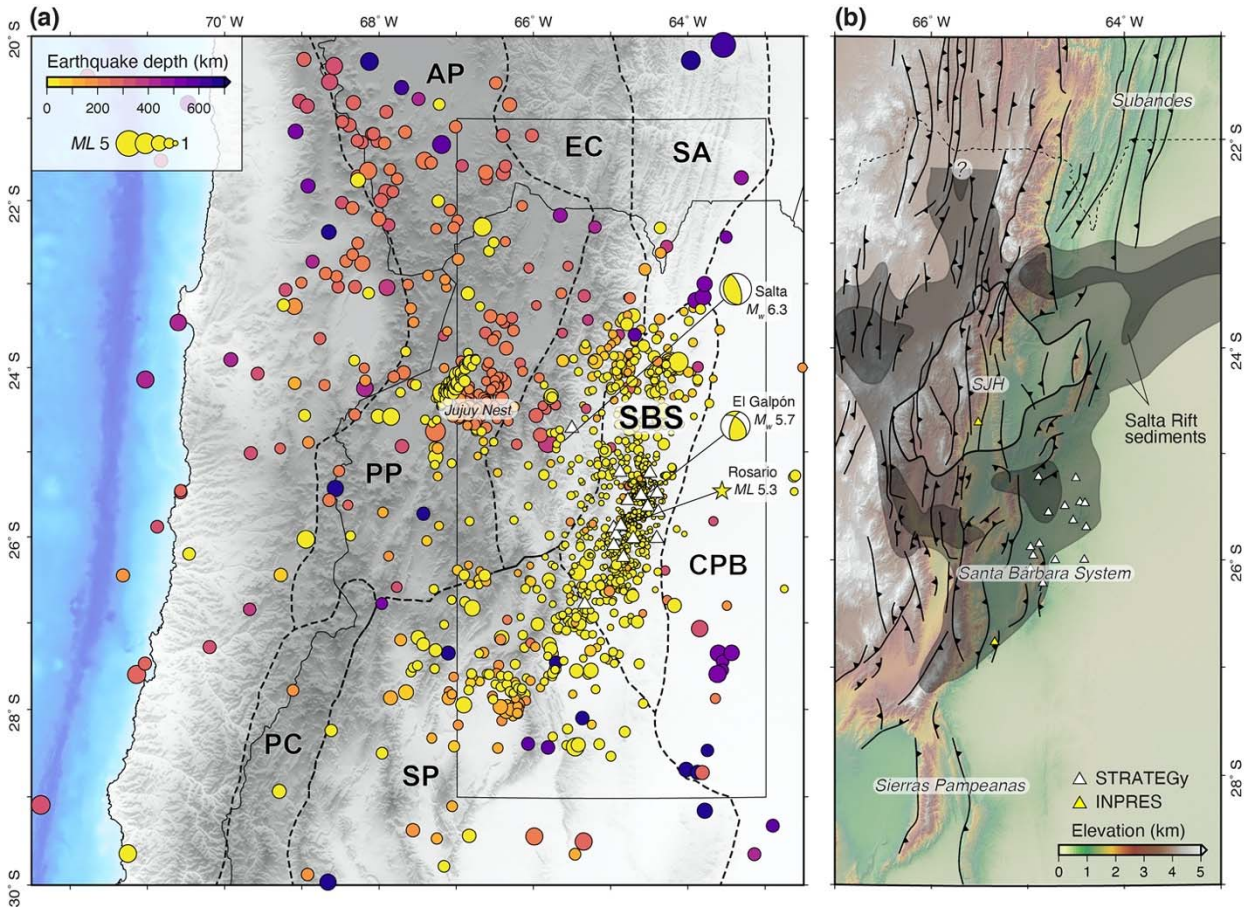

Figure 1 Seismicity and regional physiographic/tectonic structures. (a) All earthquakes recorded during the 15-month-long network deployment, color-coded by depth, and scaled to estimated local magnitudes (*ML*). Also shown is the location of the seismic network (white triangles) and the USGS focal mechanism for the 2015 El Galpón earthquake. (b) Close-up view of Cenozoic structures [*Casa et al.*, 2014; *Kley et al.*, 2005; *Mon and Salfity*, 1995; *Pingel et al.*, 2013]. Extent of the Cretaceous Salta Rift from *Kley et al.* [2005] with dark gray shading representing rift-related sediment thicknesses greater than 2000 m. White triangles are STRATEGy station locations; yellow triangles denote INPRES stations referred to in the main text. AP=Altiplano; PP=Puna Plateau; EC=Eastern Cordillera; SA=Subandes; SBS=Santa Bárbara System; SP=Sierras Pampeanas; CPB=Chaco-Paraná Basin; SJH=Salta-Jujuy High.

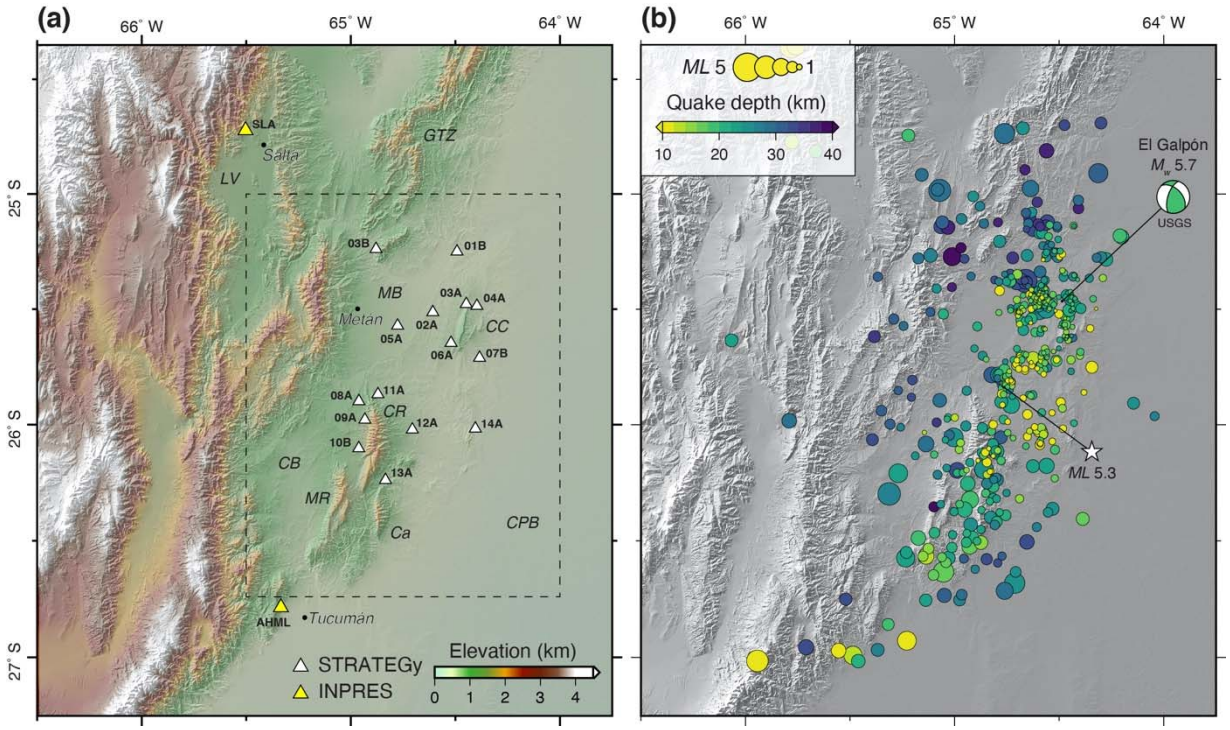

Figure 2 Local setting and relocated shallow seismicity. (a) Distribution of seismic stations used in the analysis including temporary STRATEGy installations (white triangles) and permanent stations of the Argentinian national seismological service INPRES (yellow triangles). Dashed box outlines the region shown in Figure 4a. (b) Detected and relocated local, crustal seismicity (depths ≤ 40 km) recorded during the installation period of the STRATEGy network. Circles are color-coded by depth and size is scaled to *ML*. Also shown are the USGS focal mechanism for the 2015 El Galpón earthquake and the ISC location of the preceding 2015 *ML* 5.3 Rosario de la Frontera event. GTZ=Garrapatas transverse zone; LV=Lerma Valley; MB=Metán Basin; CC=Cerro Colorado; CR=La Candelaria Range; CB=Choromoro Basin, MR=Medina Range; Ca=Campos Range, CPB=Chaco-Paraná Basin.

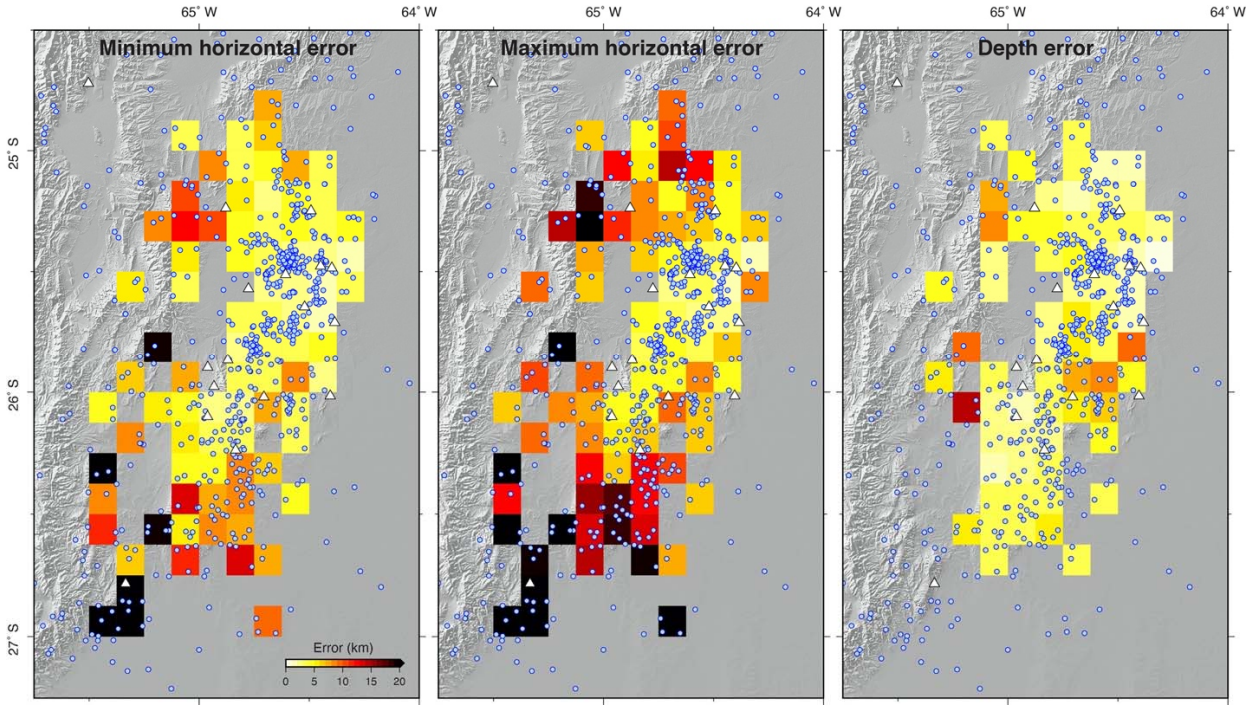

Figure 3 Quality of the STRATEGy earthquake dataset locations with event uncertainties averaged in a 0.125° x 0.125° grid; only nodes with at least two events are shown. STRATEGy and INPRES station locations are shown as white triangles and the epicenter locations for all events recorded during the network deployment are small blue circles. Errors are given as the 95% confidence interval for the location estimate. Minimum and maximum horizontal errors are defined as the semi-minor and semi-major axes of the error ellipses for the epicenter solution. Depth errors are derived independently from horizontal errors during the last location inversion step of the location, which might result in fixed event depths and a smaller number of grid nodes compared to the horizontal errors.

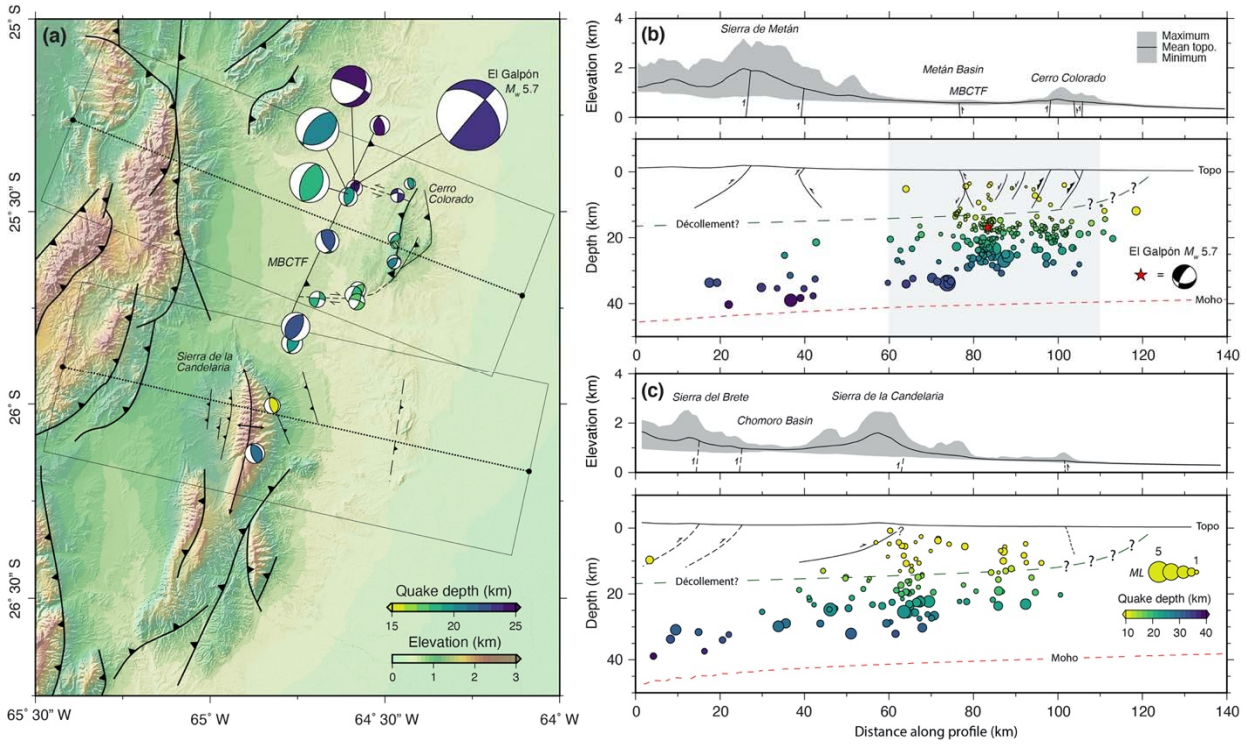

Figure 4 SBS seismotectonic map and cross-sections. (a) Topography and structures with Quaternary activity, modified after *Arnous et al.* [2020]; *Iaffa et al.* [2013]; *Iaffa et al.* [2011]; *Kley et al.* [1999]; and *Kley et al.* [2005]. Focal mechanisms derived from the first-motion polarity analysis are scaled with size to *ML* and color-coded by depth. The 2015 El Galpón event moment tensor solution from the USGS is based on teleseismic observations. The locations of the swath profiles shown in (a) are indicated with dashed lines and associated rectangles. (b) Northern profile across the Metán Basin and Cerro Colorado with vertically exaggerated swath topography and projected earthquake locations. MBCTF: Metán Basin Central Thrust Fault.; (c) Southern profile across the Choromoro Basin and Sierra de La Candelaria. Shallow subsurface fault geometries in (a) and (b) are primarily based on seismic reflection results presented in *Iaffa et al.* [2011], *Iaffa et al.* [2013], and *Arnous et al.* [2020], with fault depths typically limited to depths less than 15 km. The location of an inferred rift-related décollement is from *Grier et al.* [1991]. The Moho location in (b) and (c) is from *Tassara and Echaurren* [2012].

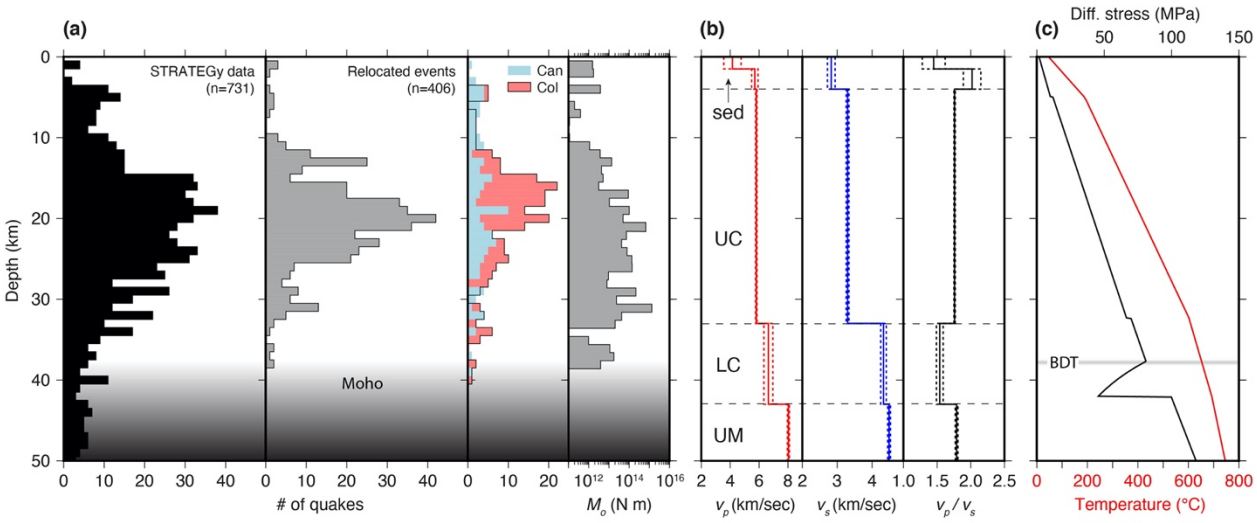

Figure 5 (a) SBS primary earthquake hypocenter depth distribution in 1 km bins from the STRATEGy deployment, relocated events (gray), relocated events for the northern SBS in the vicinity of Cerro Colorado (red) and the southern SBS in the area of the La Candelaria Range (blue), and cumulative seismic moment release with depth for the relocated catalogue based on the conversion law of *Parolai et al.* [2007]. See Figure 4 for the profile locations and Figures 1 and 2 for map views of the seismicity. (b) Seismic velocity model inverted in section XX for V_P (red), V_S (blue) and V_P/V_S ratio (black) with dashed uncertainty envelopes. sed=sediments; UC=upper crust; LC=lower crust, UM=upper mantle. (c) Yield-strength envelope (YSE; black) and temperature (red) for the southern SBS. Gray horizontal line is the location of the theoretical brittle-ductile transition (BDT) zone that coincides with the observed decrease in seismicity. Inflections in the differential stress curve indicate changes in the model rheology from a UC composed of quartzo-diorite, a LC comprised of mafic granulite, and a coefficient of friction of 0.1. See *Ibarra et al.* [2021] for more information on YSE construction.

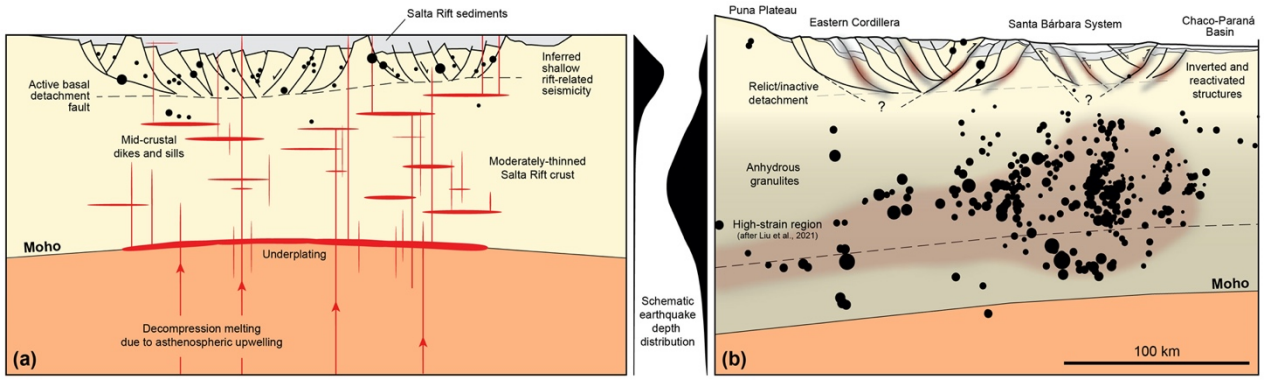

Figure 6 Conceptual model of Santa Bárbara System (SBS) deformation, rheology, and seismicity (not to scale). (a) Setting during the late Cretaceous phase of continental extension. The upper crustal cross-section with numerous Salta Rift-related normal faults that root in a shallow detachment zone are from *Grier et al.* [1991]. During the late Cretaceous, crustal thinning was accompanied by surface faulting, decompression melting, associated magmatism, and the formation of dike and sill complexes that likely caused and/or contributed to large-scale dehydration and the creation of anhydrous granulites in the middle and lower crust beneath the active rift. This view of the early rift stage of continental extension including the magmatic plumbing system and the distribution of shallow seismicity is schematic and conceptually based on studies across active rifts zones [e.g., the East African Rift System; *Albaric et al.*, 2009; *Biggs et al.*, 2021; *Corti*, 2012; *Craig and Jackson*, 2021; *Ebinger*, 2005; *Reiss et al.*, 2021]. (b) Present-day view of compressional deformation associated with Andean orogenesis. Shallow structures including inverted and reactivated faults are from *Grier et al.* [1991]. Earthquakes are from this study. The tadpole-shaped, high-strain region that generally coincides with the observed seismicity is based on the geodynamic modeling results of *Liu et al.* [2022] and is also guided by our new seismic velocity profiles and yield-strength envelope (Figure 5). The *Liu et al.* [2022] model also shows localized strain accumulation in the vicinity of the shallow structures that is separate from the deeper deformation zone. It remains unclear if and how the shallow, active faults connect to the deeper seismicity.

902

903 **References**

904 Abascal, L. d. V. (2005), Combined thin-skinned and thick-skinned deformation in the central
905 Andean foreland of northwestern Argentina, *Journal of South American Earth Sciences*, *19*(1),
906 75-81, doi:https://doi.org/10.1016/j.jsames.2005.01.004.

907 Akyol, N., L. Zhu, B. J. Mitchell, H. Sözbilir, and K. Kekovalı (2006), Crustal structure and
908 local seismicity in western Anatolia, *Geophysical Journal International*, *166*(3), 1259-1269,
909 doi:10.1111/j.1365-246X.2006.03053.x.

910 Albaric, J., J. Déverchère, C. Petit, J. Perrot, and B. Le Gall (2009), Crustal rheology and depth
911 distribution of earthquakes: Insights from the central and southern East African Rift System,
912 *Tectonophysics*, *468*(1), 28-41, doi:https://doi.org/10.1016/j.tecto.2008.05.021.

913 Allmendinger, R. W., and T. Gubbels (1996), Pure and simple shear plateau uplift, Altiplano-
914 Puna, Argentina and Bolivia, *Tectonophysics*, *259*(1), 1-13, doi:https://doi.org/10.1016/0040-
915 1951(96)00024-8.

916 Alvarado, P., and V. Ramos (2011), Earthquake deformation in the northwestern Sierras
917 Pampeanas of Argentina based on seismic waveform modeling, *Journal of Geodynamics*, *51*,
918 205-218, doi:10.1016/j.jog.2010.08.002.

919 Amitrano, D. (2003), Brittle-ductile transition and associated seismicity: Experimental and
920 numerical studies and relationship with the b value, *Journal of Geophysical Research: Solid*
921 *Earth*, *108*(B1), doi:https://doi.org/10.1029/2001JB000680.

922 Ammirati, J.-B., C. Mackaman-Lofland, M. Zeckra, and K. Gobron (2022), Stress transmission
923 along mid-crustal faults highlighted by the 2021 Mw 6.5 San Juan (Argentina) earthquake, *Sci*
924 *Rep-Uk*, *12*(1), 17939, doi:10.1038/s41598-022-22752-6.

925 Arnous, A., M. Zeckra, A. Venerdini, P. Alvarado, R. Arrowsmith, J. Guillemoteau, A. Landgraf,
926 A. Gutiérrez, and M. R. Strecker (2020), Neotectonic Activity in the Low-Strain Broken
927 Foreland (Santa Bárbara System) of the North-Western Argentinean Andes (26°S), *Lithosphere*,
928 *2020*(1), 1-25, doi:10.2113/2020/8888588.

929 Asch, G., et al. (2006), Seismological Studies of the Central and Southern Andes, in *The Andes:*
930 *Active Subduction Orogeny*, edited by O. Oncken, G. Chong, G. Franz, P. Giese, H.-J. Götze, V.
931 A. Ramos, M. R. Strecker and P. Wigger, pp. 443-457, Springer Berlin Heidelberg, Berlin,
932 Heidelberg, doi:10.1007/978-3-540-48684-8_21.

933 Babeyko, A. Y., and S. V. Sobolev (2005), Quantifying different modes of the late Cenozoic
934 shortening in the Central Andes, *Geology*, *33*(8), 621-624.

935 Barcelona, H., G. Peri, J. Tobal, L. Sagripanti, and A. Favetto (2014), Tectonic activity revealed
936 by morphostructural analysis: Development of the Sierra de la Candelaria range, northwestern
937 Argentina, *Journal of South American Earth Sciences*, *56*, 376-395,
938 doi:https://doi.org/10.1016/j.jsames.2014.10.002.

939 Behn, M. D., W. R. Buck, and I. S. Sacks (2006), Topographic controls on dike injection in
940 volcanic rift zones, *Earth Planet. Sci. Lett.*, *246*, 188-196.

941 Bellahsen, N., M. Sebrier, and L. Siame (2016), Crustal shortening at the Sierra Pie de Palo
942 (Sierras Pampeanas, Argentina): near-surface basement folding and thrusting, *Geological*
943 *Magazine*, *153*(5-6), 992-1012, doi:10.1017/S0016756816000467.

944 Beyreuther, M., R. Barsch, L. Krischer, T. Megies, Y. Behr, and J. Wassermann (2010), ObsPy: A
945 Python Toolbox for Seismology, *Seismological Research Letters*, *81*(3), 530-533,
946 doi:10.1785/gssrl.81.3.530.

947 Biggs, J., A. Ayele, T. P. Fischer, K. Fontijn, W. Hutchison, E. Kazimoto, K. Whaler, and T. J.
948 Wright (2021), Volcanic activity and hazard in the East African Rift Zone, *Nature*
949 *Communications*, *12*(1), 6881, doi:10.1038/s41467-021-27166-y.

950 Bookhagen, B., and M. Strecker (2008), Orographic barriers, high-resolution TRMM rainfall,
951 and relief variations along the eastern Andes, *Geophysical Research Letters*, *35*(L06403,),
952 doi:10.1029/2007GL032011.

953 Bormann, P., and J. W. Dewey (2012), The new IASPEI standards for determining magnitudes
954 from digital data and their relation to classical magnitudes, *New Manual of Seismological*
955 *Observatory Practice 2 (NMSOP-2)*, 1-44, doi:10.2312/GFZ.NMSOP-2_IS_3.3.

956 Brooks, B. A., M. Bevis, R. J. Smalley, E. Kendrick, R. Manceda, E. Lauria, R. Maturana, and
957 M. Araujo (2003), Crustal Motion in the Southern Andes (26°-36°S): Do the Andes Behave Like
958 a Microplate?, *Geochemistry, Geophysics, Geosystems*, *4*(10), doi:10.1029/2003GC000505.

959 Brooks, B. A., et al. (2011), Orogenic-wedge deformation and potential for great earthquakes in
960 the central Andean backarc, *Nature Geoscience*, *4*(6), 380-383, doi:Doi 10.1038/Ngeo1143.

961 Buck, W. R., L. L. Lavier, and A. N. B. Poliakov (2005), Modes of faulting at mid-ocean ridges,
962 *Nature*, *434*(7034), 719-723, doi:10.1038/nature03358.

963 Burbank, McLean, Bullen, Abdrakhmatov, and Miller (1999), Partitioning of intermontane
964 basins by thrust-related folding, Tien Shan, Kyrgyzstan, *Basin Research*, *11*(1), 75-92,
965 doi:https://doi.org/10.1046/j.1365-2117.1999.00086.x.

966 Cahill, T., and B. L. Isacks (1992), Seismicity and shape of the subducted Nazca Plate, *Journal*
967 *of Geophysical Research: Solid Earth*, *97*(B12), 17503-17529,
968 doi:https://doi.org/10.1029/92JB00493.

969 Cahill, T., B. L. Isacks, D. Whitman, J.-L. Chatelain, A. Perez, and J. M. Chiu (1992), Seismicity
970 and tectonics in Jujuy Province, northwestern Argentina, *Tectonics*, *11*(5), 944-959,
971 doi:10.1029/92tc00215.

972 Carrera, N., and J. A. Muñoz (2008), Thrusting evolution in the southern Cordillera Oriental
973 (northern Argentine Andes): Constraints from growth strata, *Tectonophysics*, *459*(1), 107-122,
974 doi:https://doi.org/10.1016/j.tecto.2007.11.068.

975 Casa, A., M. Yamin, Wright, C. Costa, M. Coppolecchia, M. Cegarra, and F. Hongn (2014),
976 Deformaciones Cuaternarias de la República Argentina, Sistema de Información Geográfica,
977 *Instituto de Geología y Recursos Minerales. Servicio Geológico Minero Argentino*, *v2.0*.

978 Cesca, S., and F. Grigoli (2015), Chapter Two - Full Waveform Seismological Advances for
979 Microseismic Monitoring, in *Advances in Geophysics*, edited by R. Dmowska, pp. 169-228,
980 Elsevier, doi:https://doi.org/10.1016/bs.agph.2014.12.002.

981 Christensen, N. I. (1996), Poisson's ratio and crustal seismology, *Journal of Geophysical*
982 *Research: Solid Earth*, *101*(B2), 3139-3156, doi:https://doi.org/10.1029/95JB03446.

983 Christensen, N. I., and W. D. Mooney (1995), Seismic velocity structure and composition of the
984 continental crust: A global view, *Journal of Geophysical Research: Solid Earth*, *100*(B6), 9761-
985 9788, doi:https://doi.org/10.1029/95JB00259.

986 Comino, J. Á. L., S. Heimann, S. Cesca, C. Milkereit, T. Dahm, and A. Zang (2017), Automated
987 Full Waveform Detection and Location Algorithm of Acoustic Emissions from Hydraulic
988 Fracturing Experiment, *Procedia Engineering*, *191*, 697-702,
989 doi:https://doi.org/10.1016/j.proeng.2017.05.234.

990 Copley, A., J.-P. Avouac, J. Hollingsworth, and S. Leprince (2011), The 2001 Mw 7.6 Bhuj
991 earthquake, low fault friction, and the crustal support of plate driving forces in India, *Journal of*
992 *Geophysical Research: Solid Earth*, *116*(B8), doi:https://doi.org/10.1029/2010JB008137.

993 Corti, G. (2012), Evolution and characteristics of continental rifting: Analog modeling-inspired
994 view and comparison with examples from the East African Rift System, *Tectonophysics*, *522-*
995 *523*, 1-33, doi:https://doi.org/10.1016/j.tecto.2011.06.010.

996 Costa, C., et al. (2020), Hazardous faults of South America; compilation and overview, *Journal*
997 *of South American Earth Sciences*, *104*, 102837,
998 doi:https://doi.org/10.1016/j.jsames.2020.102837.

999 Craig, T. J., A. Copley, and J. Jackson (2012), Thermal and tectonic consequences of India
1000 underthrusting Tibet, *Earth and Planetary Science Letters*, *353-354*, 231-239,
1001 doi:https://doi.org/10.1016/j.epsl.2012.07.010.

1002 Craig, T. J., and J. A. Jackson (2021), Variations in the Seismogenic Thickness of East Africa,
1003 *Journal of Geophysical Research: Solid Earth*, *126*(3), e2020JB020754,
1004 doi:https://doi.org/10.1029/2020JB020754.

1005 Cristallini, E., A. Cominguez, V. Ramos, and E. Mercerat (2004), Basement double-wedge
1006 thrusting in the Northern Sierras Pampeanas of Argentina (27°S) - Constraints from deep seismic
1007 reflection, edited, pp. 65-90.

1008 Cristallini, E., A. H. Cominguez, and V. A. Ramos (1997), Deep structure of the Metan-
1009 Guachipas region: tectonic inversion in Northwestern Argentina, *Journal of South American*
1010 *Earth Sciences*, *10*(5), 403-421, doi:https://doi.org/10.1016/S0895-9811(97)00026-6.

1011 Currie, C. A., and R. D. Hyndman (2006), The thermal structure of subduction zone back arcs, *J*
1012 *Geophys Res-Sol Ea*, *111*(B8), doi:10.1029/2005jb004024.

1013 Dahlen, F. A. (1990), Critical taper model of fold-and-thrust belts and accretionary wedges,
1014 *Annual Review of Earth and Planetary Sciences*, *18*, 55-99.

1015 Dahlen, F. A., J. Suppe, and D. Davis (1984), Mechanics of fold-and-thrust belts and
1016 accretionary wedges-cohesive Coulomb theory, *Journal of Geophysical Research*, *89*(NB12), 87-
1017 101, doi:10.1029/JB089iB12p10087.

1018 Davis, D., J. Suppe, and F. A. Dahlen (1983), Mechanics of fold-and-thrust belts and
1019 accretionary wedges, *Journal of Geophysical Research*, *88*(NB2), 1153-1172,
1020 doi:10.1029/JB088iB02p01153.

1021 Devlin, S., B. L. Isacks, M. E. Pritchard, W. D. Barnhart, and R. B. Lohman (2012), Depths and
1022 focal mechanisms of crustal earthquakes in the central Andes determined from teleseismic
1023 waveform analysis and InSAR, *Tectonics*, *31*(2), doi:https://doi.org/10.1029/2011TC002914.

1024 Drew, J., R. S. White, F. Tilmann, and J. Tarasewicz (2013), Coalescence microseismic mapping,
1025 *Geophysical Journal International*, *195*(3), 1773-1785, doi:10.1093/gji/ggt331.

1026 Ebinger, C. (2005), Continental break-up: The East African perspective, *Astronomy &*
1027 *Geophysics*, *46*(2), 2.16-12.21, doi:10.1111/j.1468-4004.2005.46216.x.

1028 Figueroa, S., J. R. Weiss, F. Hongn, H. Pingel, L. Escalante, L. Elías, R. G. Aranda-Viana, and
1029 M. R. Strecker (2021), Late Pleistocene to Recent Deformation in the Thick-Skinned Fold-and-
1030 Thrust Belt of Northwestern Argentina (Central Calchaquí Valley, 26°S), *Tectonics*, *40*(1),
1031 e2020TC006394, doi:https://doi.org/10.1029/2020TC006394.

1032 Franz, G., F. Lucassen, W. Kramer, R. Trumbull, R. Romer, H.-G. Wilke, J. Viramonte, R.
1033 Becchio, and W. Siebel (2006), Crustal Evolution at the Central Andean Continental Margin: a
1034 Geochemical Record of Crustal Growth, Recycling and Destruction, edited, pp. 45-64,
1035 doi:10.1007/978-3-540-48684-8_3.

1036 Galliski, M. A., and J. G. Viramonte (1988), The Cretaceous paleorift in northwestern Argentina:
1037 A petrologic approach, *Journal of South American Earth Sciences*, *1*(4), 329-342,
1038 doi:https://doi.org/10.1016/0895-9811(88)90021-1.

García, V. H., F. Hongn, and E. O. Cristallini (2013), Late Miocene to recent morphotectonic evolution and potential seismic hazard of the northern Lerma valley: Clues from Lomas de Medeiros, Cordillera Oriental, NW Argentina, *Tectonophysics*, *608*, 1238-1253, doi:https://doi.org/10.1016/j.tecto.2013.06.021.

García, V. H., F. Hongn, D. Yagupsky, H. Pingel, T. Kinnaird, D. Winocur, E. Cristallini, R. A. J. Robinson, and M. R. Strecker (2019), Late Quaternary tectonics controlled by fault reactivation. Insights from a local transpressional system in the intermontane Lerma valley, Cordillera Oriental, NW Argentina, *Journal of Structural Geology*, *128*, 103875, doi:https://doi.org/10.1016/j.jsg.2019.103875.

Gioncada, A., L. Vezzoli, M. R, R. Omarini, P. Nonnotte, and H. Guillou (2010), Pliocene intraplate-type volcanism in the Andean foreland at 26°10′S, 64°40′W (NW Argentina): Implications for magmatic and structural evolution of the Central Andes, *Lithosphere*, *2*, 153-171, doi:10.1130/L81.1.

Grier, M. E., J. A. Salfity, and R. W. Allmendinger (1991), Andean reactivation of the Cretaceous Salta rift, northwestern Argentina, *Journal of South American Earth Sciences*, *4*(4), 351-372, doi:https://doi.org/10.1016/0895-9811(91)90007-8.

Grigoli, F., S. Cesca, M. Vassallo, and T. Dahm (2013), Automated Seismic Event Location by Travel-Time Stacking: An Application to Mining Induced Seismicity, *Seismological Research Letters*, *84*(4), 666-677, doi:10.1785/0220120191.

Gubbels, T. L., B. L. Isacks, and E. Farrar (1993), High-level surfaces, plateau uplift, and foreland development, Bolivian Central Andes, *Geology*, *21*(8), 695-698.

Hain, M. P., M. R. Strecker, B. Bookhagen, R. N. Alonso, H. Pingel, and A. K. Schmitt (2011), Neogene to Quaternary broken foreland formation and sedimentation dynamics in the Andes of NW Argentina (25°S), *Tectonics*, *30*(2), doi:10.1029/2010tc002703.

Heimann, S., H. Vasyura-Bathke, H. Sudhaus, M. P. Isken, M. Kriegerowski, A. Steinberg, and T. Dahm (2019), A Python framework for efficient use of pre-computed Green's functions in seismological and other physical forward and inverse source problems, *Solid Earth*, *10*(6), 1921-1935, doi:10.5194/se-10-1921-2019.

Hibert, C., et al. (2014), Automated identification, location, and volume estimation of rockfalls at Piton de la Fournaise volcano, *Journal of Geophysical Research: Earth Surface*, *119*(5), 1082-1105, doi:https://doi.org/10.1002/2013JF002970.

Hilley, G. E., P. M. Blisniuk, and M. R. Strecker (2005), Mechanics and erosion of basement-cored uplift provinces, *Journal of Geophysical Research: Solid Earth*, *110*(B12), doi:10.1029/2005jb003704.

1073 Hilley, G. E., and M. R. Strecker (2004), Steady state erosion of critical Coulomb wedges with
1074 applications to Taiwan and the Himalaya, *J Geophys Res-Sol Ea*, *109*(B1),
1075 doi:10.1029/2002jb002284.

1076 Husen, S., E. Kissling, N. Deichmann, S. Wiemer, D. Giardini, and M. Baer (2003), Probabilistic
1077 earthquake location in complex three-dimensional velocity models: Application to Switzerland,
1078 *Journal of Geophysical Research: Solid Earth*, *108*(B2),
1079 doi:https://doi.org/10.1029/2002JB001778.

1080 Iaffa, D., F. Sàbat, J. Muñoz, and N. Carrera (2013), Basin fragmentation controlled by tectonic
1081 inversion and basement uplift in Sierras Pampeanas and Santa Bárbara System, northwest
1082 Argentina, *Geological Society London Special Publications*, *377*, doi:10.1144/SP377.13.

1083 Iaffa, D. N., F. Sàbat, J. A. Muñoz, R. Mon, and A. A. Gutierrez (2011), The role of inherited
1084 structures in a foreland basin evolution. The Metán Basin in NW Argentina, *Journal of Structural*
1085 *Geology*, *33*(12), 1816-1828, doi:https://doi.org/10.1016/j.jsg.2011.09.005.

1086 Ibarra, F., S. Liu, C. Meeßen, C. B. Prezzi, J. Bott, M. Scheck-Wenderoth, S. Sobolev, and M. R.
1087 Strecker (2019), 3D data-derived lithospheric structure of the Central Andes and its implications
1088 for deformation: Insights from gravity and geodynamic modelling, *Tectonophysics*, *766*, 453-
1089 468, doi:https://doi.org/10.1016/j.tecto.2019.06.025.

1090 Ibarra, F., C. B. Prezzi, J. Bott, M. Scheck-Wenderoth, and M. R. Strecker (2021), Distribution of
1091 Temperature and Strength in the Central Andean Lithosphere and Its Relationship to Seismicity
1092 and Active Deformation, *Journal of Geophysical Research: Solid Earth*, *126*(5),
1093 e2020JB021231, doi:https://doi.org/10.1029/2020JB021231.

1094 Jackson, J., K. Priestley, and B. Emmerson (2008), New views on the structure and rheology of
1095 the lithosphere, *Journal of the Geological Society*, *165*(2), 453-465, doi:10.1144/0016-
1096 76492007-109.

1097 Jackson, J. A., H. Austrheim, D. McKenzie, and K. Priestley (2004), Metastability, mechanical
1098 strength, and the support of mountain belts, *Geology*, *32*(7), 625-628, doi:10.1130/g20397.1.

1099 Jordan, T. E., and R. W. Allmendinger (1986), The Sierras Pampeanas of Argentina; a modern
1100 analogue of Rocky Mountain foreland deformation, *American Journal of Science*, *286*, 737-764,
1101 doi:10.2475/ajs.286.10.737.

1102 Jordan, T. E., B. L. Isacks, R. W. Allmendinger, J. A. Brewer, V. A. Ramos, and C. J. Ando
1103 (1983), Andean tectonics related to geometry of subducted Nazca plate, *GSA Bulletin*, *94*(3),
1104 341-361, doi:10.1130/0016-7606(1983)94<341:Atrtgo>2.0.Co;2.

1105 Kennett, B. L. N., E. R. Engdahl, and R. Buland (1995), Constraints on seismic velocities in the
1106 Earth from traveltimes, *Geophysical Journal International*, *122*(1), 108-124, doi:10.1111/j.1365-
1107 246X.1995.tb03540.x.

1108 Kirby, S., R. E. Engdahl, and R. Denlinger (1996), Intermediate-Depth Intraslab Earthquakes and
1109 Arc Volcanism as Physical Expressions of Crustal and Uppermost Mantle Metamorphism in
1110 Subducting Slabs, in *Subduction*, edited, pp. 195-214, doi:https://doi.org/10.1029/GM096p0195.

1111 Kissling, E., W. L. Ellsworth, D. Eberhart-Phillips, and U. Kradolfer (1994), Initial reference
1112 models in local earthquake tomography, *Journal of Geophysical Research: Solid Earth*, *99*(B10),
1113 19635-19646, doi:https://doi.org/10.1029/93JB03138.

1114 Kley, J., and C. R. Monaldi (2002), Tectonic inversion in the Santa Barbara System of the central
1115 Andean foreland thrust belt, northwestern Argentina, *Tectonics*, *21*(6), 11-11-11-18,
1116 doi:10.1029/2002tc902003.

1117 Kley, J., C. R. Monaldi, and J. Salfity (1996), *Along-strike segmentation of the Andean foreland*.

1118 Kley, J., C. R. Monaldi, and J. A. Salfity (1999), Along-strike segmentation of the Andean
1119 foreland; causes and consequences, *Tectonophysics*, *301*(1-2), 75-94.

1120 Kley, J., E. A. Rossello, C. R. Monaldi, and B. Habighorst (2005), Seismic and field evidence for
1121 selective inversion of Cretaceous normal faults, Salta rift, northwest Argentina, *Tectonophysics*,
1122 *399*(1), 155-172, doi:https://doi.org/10.1016/j.tecto.2004.12.020.

1123 Lacombe, O., and N. Bellahsen (2016), Thick-skinned tectonics and basement-involved fold–
1124 thrust belts: insights from selected Cenozoic orogens, *Geological Magazine*, *153*(5-6), 763-810,
1125 doi:10.1017/S0016756816000078.

1126 Lamb, S. (2000), Active deformation in the Bolivian Andes, South America, *Journal of*
1127 *Geophysical Research*, *105*(B11), 25,627-625,653.

1128 Langet, N., A. Maggi, A. Michelini, and F. Brenguier (2014), Continuous Kurtosis-Based
1129 Migration for Seismic Event Detection and Location, with Application to Piton de la Fournaise
1130 Volcano, La Réunion, *Bulletin of the Seismological Society of America*, *104*(1), 229-246,
1131 doi:10.1785/0120130107.

1132 Laske, G., G. Masters, Z. Ma, and M. Pasyanos (2013), Update on CRUST1.0 - A 1-degree
1133 global model of Earth's crust, *Abstract EGU2013-2658 presented at 2013 Geophys. Res.*
1134 *Abstracts 15*, *15*, 2658.

1135 Liu, S., S. V. Sobolev, A. Y. Babeyko, and M. V. Pons-Rallo (2022), Controls of the Foreland
1136 Deformation Pattern in the Orogen-Foreland Shortening System: Constraints from High-
1137 Resolution Geodynamic Models, *Earth and Space Science Open Archive*, 35,
1138 doi:doi:10.1002/essoar.10508507.2.

1139 Lucassen, F., G. Franz, R. Romer, F. Schultz, P. Dulski, and K. Wemmer (2007), Pre-Cenozoic
1140 intra-plate magmatism along the Central Andes (17–34°S): Composition of the mantle at an
1141 active margin, *Lithos*, *99*, 312-338, doi:10.1016/j.lithos.2007.06.007.

1142 Lucassen, F., G. Franz, J. Viramonte, R. L. Romer, P. Dulski, and A. Lang (2005), The late
1143 Cretaceous lithospheric mantle beneath the Central Andes: Evidence from phase equilibria and
1144 composition of mantle xenoliths, *Lithos*, *82*, 379-406, doi:10.1016/j.lithos.2004.08.002.

1145 Lucassen, F., S. Lewerenz, G. Franz, J. Viramonte, and K. Mezger (1999), Metamorphism,
1146 isotopic ages and composition of lower crustal granulite xenoliths from the Cretaceous Salta Rift,
1147 Argentina, *Contributions to Mineralogy and Petrology*, *134*, 325, doi:10.1007/s004100050488.

1148 Maggi, A., J. A. Jackson, D. McKenzie, and K. Priestley (2000), Earthquake focal depths,
1149 effective elastic thickness, and the strength of the continental lithosphere, *Geology*, *28*(6), 495-
1150 498, doi:10.1130/0091-7613(2000)28<495:Efdeet>2.0.Co;2.

1151 Marquillas, R. A., C. del Papa, and I. F. Sabino (2005), Sedimentary aspects and
1152 paleoenvironmental evolution of a rift basin: Salta Group (Cretaceous–Paleogene), northwestern
1153 Argentina, *Int J Earth Sci*, *94*(1), 94-113, doi:10.1007/s00531-004-0443-2.

1154 Marshak, S., K. Karlstrom, and J. M. Timmons (2000), Inversion of Proterozoic extensional
1155 faults: An explanation for the pattern of Laramide and Ancestral Rockies intracratonic
1156 deformation, United States, *Geology*, *28*(8), 735-738, doi:10.1130/0091-
1157 7613(2000)28<735:Iopefa>2.0.Co;2.

1158 McFarland, P. K., R. A. Bennett, P. Alvarado, and P. G. DeCelles (2017), Rapid Geodetic
1159 Shortening Across the Eastern Cordillera of NW Argentina Observed by the Puna-Andes GPS
1160 Array, *Journal of Geophysical Research: Solid Earth*, *122*(10), 8600-8623,
1161 doi:10.1002/2017jb014739.

1162 Michailos, K., E. G. C. Smith, C. J. Chamberlain, M. K. Savage, and J. Townend (2019),
1163 Variations in Seismogenic Thickness Along the Central Alpine Fault, New Zealand, Revealed by
1164 a Decade's Relocated Microseismicity, *Geochemistry, Geophysics, Geosystems*, *20*(1), 470-486,
1165 doi:https://doi.org/10.1029/2018GC007743.

1166 Mon, R. (1976), The structure of the eastern border of the Andes in north-western Argentina,
1167 *Geologische Rundschau*, *65*(1), 211-222, doi:10.1007/BF01808464.

1168 Mon, R., and A. A. Gutiérrez (2007), Estructura del extremo sur del sistema subandino
1169 (provincias de Salta, Santiago del Estero y Tucumán), *Revista de la Asociación Geológica*
1170 *Argentina*, *62*(1), 62-68.

1171 Mon, R., and J. A. Salfity (1995), Tectonic Evolution of the Andes of Northern Argentina, in
1172 *Petroleum Basins of South America*, edited by A. J. Tankard, R. S. Soruco and H. J. Welsink, pp.
1173 269-283, American Association of Petroleum Geologists, doi:10.1306/m62593c12.

1174 Monsalve, G., J. S. Jaramillo, A. Cardona, V. Schulte-Pelkum, G. Posada, V. Valencia, and E.
1175 Poveda (2019), Deep Crustal Faults, Shear Zones, and Magmatism in the Eastern Cordillera of
1176 Colombia: Growth of a Plateau From Teleseismic Receiver Function and Geochemical Mio-

1177 Pliocene Volcanism Constraints, *Journal of Geophysical Research: Solid Earth*, *124*(9), 9833-
1178 9851, doi:https://doi.org/10.1029/2019JB017835.

1179 Monsalve, G., A. Sheehan, V. Schulte-Pelkum, S. Rajaure, M. R. Pandey, and F. Wu (2006),
1180 Seismicity and one-dimensional velocity structure of the Himalayan collision zone: Earthquakes
1181 in the crust and upper mantle, *Journal of Geophysical Research: Solid Earth*, *111*(B10),
1182 doi:https://doi.org/10.1029/2005JB004062.

1183 Mori, J., and R. E. Abercrombie (1997), Depth dependence of earthquake frequency-magnitude
1184 distributions in California: Implications for rupture initiation, *Journal of Geophysical Research:*
1185 *Solid Earth*, *102*(B7), 15081-15090, doi:https://doi.org/10.1029/97JB01356.

1186 Mulcahy, P., C. Chen, S. M. Kay, L. D. Brown, B. L. Isacks, E. Sandvol, B. Heit, X. Yuan, and B.
1187 L. Coira (2014), Central Andean mantle and crustal seismicity beneath the Southern Puna plateau
1188 and the northern margin of the Chilean-Pampean flat slab, *Tectonics*, *33*(8), 1636-1658,
1189 doi:https://doi.org/10.1002/2013TC003393.

1190 Ortiz, G., A. L. Stevens Goddard, J. C. Fosdick, P. Alvarado, B. Carrapa, and E. Cristofolini
1191 (2021), Fault reactivation in the Sierras Pampeanas resolved across Andean extensional and
1192 compressional regimes using thermochronologic modeling, *Journal of South American Earth*
1193 *Sciences*, *112*, 103533, doi:https://doi.org/10.1016/j.jsames.2021.103533.

1194 Parolai, S., D. Bindi, E. Durukal, H. Grosser, and C. Milkereit (2007), Source Parameters and
1195 Seismic Moment–Magnitude Scaling for Northwestern Turkey, *Bulletin of the Seismological*
1196 *Society of America*, *97*(2), 655-660, doi:10.1785/0120060180.

1197 Pearson, D. M., P. Kapp, P. G. DeCelles, P. W. Reiners, G. E. Gehrels, M. N. Ducea, and A.
1198 Pullen (2013), Influence of pre-Andean crustal structure on Cenozoic thrust belt kinematics and
1199 shortening magnitude: Northwestern Argentina, *Geosphere*, *9*(6), 1766-1782,
1200 doi:10.1130/ges00923.1.

1201 Perucca, L., and S. Moreiras (2009), Seismic and Volcanic Hazards in Argentina, *Developments*
1202 *in Earth Surface Processes*, *13*, doi:10.1016/S0928-2025(08)10014-1.

1203 Pingel, H., M. R. Strecker, R. N. Alonso, and A. K. Schmitt (2013), Neotectonic basin and
1204 landscape evolution in the Eastern Cordillera of NW Argentina, Humahuaca Basin (~24°S),
1205 *Basin Research*, *25*(5), 554-573, doi:https://doi.org/10.1111/bre.12016.

1206 Pugh, D., and R. White (2018), MTfit: A Bayesian Approach to Seismic Moment Tensor
1207 Inversion, *Seismological Research Letters*, *89*, doi:10.1785/0220170273.

1208 Pugh, D. J., R. S. White, and P. A. F. Christie (2016), A Bayesian method for microseismic
1209 source inversion, *Geophysical Journal International*, *206*(2), 1009-1038,
1210 doi:10.1093/gji/ggw186.

1211 Ramezani Ziarani, M., B. Bookhagen, T. Schmidt, J. Wickert, A. de la Torre, and R. Hierro
1212 (2019), Using Convective Available Potential Energy (CAPE) and Dew-Point Temperature to
1213 Characterize Rainfall-Extreme Events in the South-Central Andes, *Atmosphere*, *10*(7), 379.

1214 Ramos, V. (1988), The tectonics of the Central Andes; 30 to 33 S latitude, *Special Paper of the*
1215 *Geological Society of America*, *218*, 31-54, doi:10.1130/SPE218-p31.

1216 Ramos, V. (2000), Las provincias geológicas del territorio argentino, *Geología Argentina*, *29*, 41-
1217 96.

1218 Ramos, V. A., R. Alonso, and M. Strecker (2006), Estructura y neotectónica de Las Lomas de
1219 Olmedo, zona de transición entre los Sistemas Subandino y de Santa Bárbara, provincia de Salta,
1220 *Revista de la Asociacion Geologica Argentina*, *61*, 579-588.

1221 Ramos, V. A., E. O. Cristallini, and D. J. Pérez (2002), The Pampean flat-slab of the Central
1222 Andes, *Journal of South American Earth Sciences*, *15*(1), 59-78,
1223 doi:https://doi.org/10.1016/S0895-9811(02)00006-8.

1224 Ramos, V. A., T. Zapata, E. Cristallini, and A. Introcaso (2004), The Andean thrust system-
1225 Latitudinal variations in structural styles and orogenic shortening, in *Thrust tectonics and*
1226 *hydrocarbon systems: AAPG Memoir 82*, edited by K. R. McClay, pp. 30-50.

1227 Rapela, C. W., R. J. Pankhurst, C. Casquet, E. Baldo, C. Galindo, C. M. Fanning, and J. M.
1228 Dahlquist (2010), The Western Sierras Pampeanas: Protracted Grenville-age history (1330–
1229 1030Ma) of intra-oceanic arcs, subduction–accretion at continental-edge and AMCG intraplate
1230 magmatism, *Journal of South American Earth Sciences*, *29*(1), 105-127,
1231 doi:https://doi.org/10.1016/j.jsames.2009.08.004.

1232 Reiss, M. C., J. D. Muirhead, A. S. Laizer, F. Link, E. O. Kazimoto, C. J. Ebinger, and G.
1233 Rümpker (2021), The Impact of Complex Volcanic Plumbing on the Nature of Seismicity in the
1234 Developing Magmatic Natron Rift, Tanzania, *Frontiers in Earth Science*, *8*,
1235 doi:10.3389/feart.2020.609805.

1236 Sánchez, G., R. Recio, O. Marcuzzi, M. Moreno, M. Araujo, C. Navarro, J. C. Suárez, J.
1237 Havskov, and L. Ottemöller (2013), The Argentinean National Network of Seismic and Strong-
1238 Motion Stations, *Seismological Research Letters*, *84*(5), 729-736, doi:10.1785/0220120045.

1239 Scholz, C. J. (1998), Earthquakes and friction laws, *Nature*, *391*, 37-42.

1240 Schorlemmer, D., F. Euchner, P. Kästli, and J. Saul (2011), QuakeML: status of the XML-based
1241 seismological data exchange format, *2011*, *54*(1), 7, doi:10.4401/ag-4874.

1242 Schurr, B., G. Asch, A. Rietbrock, R. Kind, M. Pardo, B. Heit, and T. Monfret (1999), Seismicity
1243 and average velocities beneath the Argentine Puna Plateau, *Geophysical Research Letters*,
1244 *26*(19), 3025-3028, doi:https://doi.org/10.1029/1999GL005385.

1245 Schurr, B., G. Asch, A. Rietbrock, R. Trumbull, and C. Haberland (2003), Complex patterns of
1246 fluid and melt transport in the central Andean subduction zone revealed by attenuation
1247 tomography, *Earth and Planetary Science Letters*, *215*(1–2), 105-119,
1248 doi:http://dx.doi.org/10.1016/S0012-821X(03)00441-2.

1249 Schurr, B., L. Ratschbacher, C. Sippl, R. Gloaguen, X. Yuan, and J. Mechie (2014),
1250 Seismotectonics of the Pamir, *Tectonics*, *33*(8), 1501-1518,
1251 doi:https://doi.org/10.1002/2014TC003576.

1252 Schweitzer, J. (2001), HYPOSAT – An Enhanced Routine to Locate Seismic Events, *pure and*
1253 *applied geophysics*, *158*(1), 277-289, doi:10.1007/PL00001160.

1254 Scott, C., R. Lohman, M. Pritchard, P. Alvarado, and G. Sánchez (2014), Andean earthquakes
1255 triggered by the 2010 Maule, Chile (Mw 8.8) earthquake: Comparisons of geodetic, seismic and
1256 geologic constraints, *Journal of South American Earth Sciences*, *50*, 27-39,
1257 doi:https://doi.org/10.1016/j.jsames.2013.12.001.

1258 Seagren, E. G., M. McMillan, and L. M. Schoenbohm (2022), Tectonic Control on Drainage
1259 Evolution in Broken Forelands: Examples From NW Argentina, *Tectonics*, *41*(1),
1260 e2020TC006536, doi:https://doi.org/10.1029/2020TC006536.

1261 Sibson, R. H. (1982), Fault zone models, heat flow, and the depth distribution of earthquakes in
1262 the continental crust of the United States, *Bulletin of the Seismological Society of America*, *72*(1),
1263 151-163, doi:10.1785/bssa0720010151.

1264 Sippl, C., et al. (2013), Geometry of the Pamir-Hindu Kush intermediate-depth earthquake zone
1265 from local seismic data, *Journal of Geophysical Research: Solid Earth*, *118*(4), 1438-1457,
1266 doi:https://doi.org/10.1002/jgrb.50128.

1267 Sloan, R. A., J. A. Jackson, D. McKenzie, and K. Priestley (2011), Earthquake depth
1268 distributions in central Asia, and their relations with lithosphere thickness, shortening and
1269 extension, *Geophysical Journal International*, *185*(1), 1-29, doi:10.1111/j.1365-
1270 246X.2010.04882.x.

1271 Smalley Jr., R., J. Pujol, M. Regnier, J. M. Chiu, J. L. Chatelain, B. Isacks, M. Araujo, and N.
1272 Puebla (1993), Basement seismicity beneath the Andean precordillera thin-skinned thrust belt
1273 and implications for crustal and lithospheric behavior, *Tectonics*, *12*(1), 63-76,
1274 doi:https://doi.org/10.1029/92TC01108.

1275 Storchak, D. A., J. Schweitzer, and P. Bormann (2003), The IASPEI Standard Seismic Phase
1276 List, *Seismological Research Letters*, *74*(6), 761-772, doi:10.1785/gssrl.74.6.761.

1277 Strecker, M. R., R. N. Alonso, B. Bookhagen, B. Carrapa, G. E. Hilley, E. R. Sobel, and M. H.
1278 Trauth (2007), Tectonics and Climate of the Southern Central Andes, *Annual Review of Earth*
1279 *and Planetary Sciences*, *35*(1), 747-787, doi:10.1146/annurev.earth.35.031306.140158.

1280 Strecker, M. R., G. E. Hilley, B. Bookhagen, and E. R. Sobel (2012), Structural, Geomorphic,
1281 and Depositional Characteristics of Contiguous and Broken Foreland Basins: Examples from the
1282 Eastern Flanks of the Central Andes in Bolivia and NW Argentina, in *Tectonics of Sedimentary*
1283 *Basins*, edited, pp. 508-521, doi:10.1002/9781444347166.ch25.

1284 Taboada, A., L. A. Rivera, A. Fuenzalida, A. Cisternas, H. Philip, H. Bijwaard, J. Olaya, and C.
1285 Rivera (2000), Geodynamics of the northern Andes: Subductions and intracontinental
1286 deformation (Colombia), *Tectonics*, *19*(5), 787-813, doi:https://doi.org/10.1029/2000TC900004.

1287 Tassara, A., and A. Echaurren (2012), Anatomy of the Andean subduction zone: three-
1288 dimensional density model upgraded and compared against global-scale models, *Geophysical*
1289 *Journal International*, *189*(1), 161-168, doi:doi:10.1111/j.1365-246X.2012.05397.x.

1290 Tongue, J. A., P. K. H. Maguire, and P. A. V. Young (1992), Seismicity distribution from
1291 temporary earthquake recording networks in Kenya, *Tectonophysics*, *204*(1-2), 71-79,
1292 doi:10.1016/0040-1951(92)90270-g.

1293 Utsu, T., Y. Ogata, S. Ritsuko, and Matsu-ura (1995), The Centenary of the Omori Formula for a
1294 Decay Law of Aftershock Activity, *Journal of physics of the earth*, *43*, 1-33.

1295 Valenzuela-Malebrán, C., S. Cesca, J. A. López-Comino, M. Zeckra, F. Krüger, and T. Dahm
1296 (2022), Source mechanisms and rupture processes of the Jujuy seismic nest, Chile-Argentina
1297 border, *Journal of South American Earth Sciences*, *117*, 103887,
1298 doi:https://doi.org/10.1016/j.jsames.2022.103887.

1299 Vásquez, M., and U. Altenberger (2005), Mid-Cretaceous extension-related magmatism in the
1300 eastern Colombian Andes, *Journal of South American Earth Sciences*, *20*(3), 193-210,
1301 doi:https://doi.org/10.1016/j.jsames.2005.05.010.

1302 Viramonte, J. G., S. M. Kay, R. Becchio, M. Escayola, and I. Novitski (1999), Cretaceous rift
1303 related magmatism in central-western South America, *Journal of South American Earth*
1304 *Sciences*, *12*(2), 109-121, doi:https://doi.org/10.1016/S0895-9811(99)00009-7.

1305 Waldhauser, F., and W. L. Ellsworth (2000), A Double-difference Earthquake location algorithm:
1306 Method and application to the Northern Hayward Fault, California, *Bulletin of the Seismological*
1307 *Society of America*, *90*(6), 1353-1368, doi:10.1785/0120000006.

1308 Weber, M., J. Tarney, P. Kempton, and R. Kent (2002), Crustal make-up of the Northern Andes:
1309 Evidence based on deep crustal xenolith suites, Mercaderes, SW Colombia, *Tectonophysics*, *345*,
1310 49-82, doi:10.1016/S0040-1951(01)00206-2.

1311 Weiss, J. R., et al. (2016), Isolating active orogenic wedge deformation in the southern Subandes
1312 of Bolivia, *Journal of Geophysical Research: Solid Earth*, *121*(8), 6192-6218,
1313 doi:10.1002/2016JB013145.

1314 Weiss, J. R., G. Ito, B. A. Brooks, J.-A. Olive, J. H. Foster, and G. F. Moore (2018), Formation of
1315 the frontal zone of accretionary wedges, *Earth and Planetary Science Letters*, *495*, 87-100,
1316 doi:10.1016/j.epsl.2018.05.010.

1317 Wessel, P., W. H. F. Smith, R. Scharroo, J. Luis, and F. Wobbe (2013), Generic Mapping Tools:
1318 Improved Version Released, *Eos, Transactions American Geophysical Union*, *94*(45), 409-410,
1319 doi:10.1002/2013EO450001.

1320 Whitman, D. (1994), Moho geometry beneath the eastern margin of the Andes, northwest
1321 Argentina, and its implications to the effective elastic thickness of the Andean foreland, *J*
1322 *Geophys Res-Sol Ea*, *99*(B8), 15277-15289, doi:10.1029/94jb00342.

1323 Whitman, D., B. L. Isacks, J. L. Chatelain, J. M. Chiu, and A. Perez (1992), Attentuation of high-
1324 frequency seismic-waves beneath the central Andean plateau, *J Geophys Res-Sol Ea*, *97*(B13),
1325 19929-19947, doi:10.1029/92jb01748.

1326 Willett, S. D. (1999), Orogeny and orography: The effects of erosion on the structure of
1327 mountain belts, *J Geophys Res-Sol Ea*, *104*(B12), 28957-28981, doi:Doi 10.1029/1999jb900248.

1328 Wimpenny, S. (2022), Weak, Seismogenic Faults Inherited From Mesozoic Rifts Control
1329 Mountain Building in the Andean Foreland, *Geochemistry, Geophysics, Geosystems*, *23*,
1330 e2021GC010270, doi:10.1029/2021GC010270.

1331 Wimpenny, S., A. Copley, C. Benavente, and E. Aguirre (2018), Extension and Dynamics of the
1332 Andes Inferred From the 2016 Parina (Huarichancara) Earthquake, *Journal of Geophysical*
1333 *Research: Solid Earth*, *123*(9), 8198-8228, doi:10.1029/2018jb015588.

1334 Woessner, J., and S. Wiemer (2005), Assessing the Quality of Earthquake Catalogues: Estimating
1335 the Magnitude of Completeness and Its Uncertainty, *Bulletin of the Seismological Society of*
1336 *America*, *95*(2), 684-698, doi:10.1785/0120040007.

1337 Yardley, B. W. D., and J. W. Valley (1997), The petrologic case for a dry lower crust, *Journal of*
1338 *Geophysical Research: Solid Earth*, *102*(B6), 12173-12185, doi:doi.org/10.1029/97JB00508.

1339 Zeckra, M. (2020), Seismological and Seismotectonic Analysis of the Northwestern Argentine
1340 Central Andean Foreland, 120 pp, University of Potsdam, Potsdam, Germany.

1341 Zeckra, M., and F. Kruger (2016), Seismic neTwoRk/Array in norThwEstern arGentina, edited,
1342 International Federation of Digital Seismograph Networks, doi:10.7914/SN/2S_2016.

1343 Zoback, M. D., et al. (1987), New Evidence on the State of Stress of the San Andreas Fault
1344 System, *Science*, *238*(4830), 1105-1111, doi:doi:10.1126/science.238.4830.1105.

1345 Zossi, M. M. (1979), Estudio de la actividad sismica de la Privincia de Tucuman, doctoral thesis,
1346 125 pp, Universidad Nacional de Tucuman.
1347